

Supporting Information:

Low density interior in supercooled aqueous nanodroplets expels ions to the subsurface

Shahrazad M. A. Malek,[†] Victor Kwan,[‡] Ivan Saika-Voivod,[†] and Styliani Consta^{*,‡}

[†] *Department of Physics and Physical Oceanography, Memorial University of Newfoundland, Canada, A1B 3X7*

[‡] *Department of Chemistry, The University of Western Ontario, London, Ontario, Canada N6A 5B7*

[¶] *Department of Applied Mathematics, Western University, London, Ontario, Canada, N6A 3K7*

E-mail: sconstas@uwo.ca

S1. Details of the analytical model of a single ion location within a fluctuating droplet

Here we discuss details of the analytical model that predicts a simple ion's or macroion's location in a fluctuating droplet. The key points of the model are presented in the main text.

The following discussion is an extension of our previous work on the energy of a continuum dielectric droplet containing a single (macro)ion.^{S1,S2} In the model the droplet surface fluctuations are considered. The total energy of the droplet (E) is written as the sum of surface energy (E_{surf}) and electrostatic energy (E_{el}),^{S2,S3}

$$E = E_{\text{surf}} + E_{\text{el}} = \gamma A + E_{\text{el}} \quad (\text{S1})$$

where γ is the surface tension and A surface area. E_{el} is given by

$$E_{\text{el}} = -\frac{1}{2} \int_{\mathbb{R}^3/V} d\mathbf{r} (\epsilon^E - \epsilon^I) \mathbf{E} \cdot \mathbf{E}_0 \quad (\text{S2})$$

where \mathbb{R}^3/V are the points in the exterior of the droplet, ϵ^I is the electric permittivity in the interior of a droplet, ϵ^E is the electric permittivity of the medium surrounding the droplet, and

$$\mathbf{E}_0(\mathbf{r}) = -\nabla \frac{Q}{4\pi\epsilon^I r}. \quad (\text{S3})$$

The distance of a point on the droplet surface from the ion is given by:

$$\rho(\sigma) = R + \sum_{l>0, m_l} a_{l, m_l} Y_{l, m_l}(\sigma) \quad (\text{S4})$$

where $\sigma = (\theta, \phi)$ is the spherical angle, $\rho(\theta, \phi)$ is the distance from the centre (which is at the ion), and $Y_{lm}(\theta, \phi)$ denote the spherical harmonics functions of rank m and order l . For

certain shapes of droplets, such as bottle-necked shapes or shapes like an eight we should choose the center of the shape carefully, so as we do not have for a single (θ, ϕ) more than one values of ρ . In other words, the same line intersects the shape in several points. R is the $l = 0$ term in the expansion of $\rho(\sigma)$. The details of the algebra for expressing E_{surf} in terms of the expansion coefficients a_{l,m_l} (see Eq. S4) is given in Ref.[^{S1}]. The coupling of the electrostatic energy^{S4} to the shape fluctuations is a tedious step and one of the ways to do that is found in Ref.[^{S2}].

After some algebra, the total energy is given by

$$E = \frac{(\epsilon^I - \epsilon^E)Q^2}{8\pi\epsilon^I\epsilon^E R_0} \left[1 - \sum_{l>0,m_l} \frac{\epsilon^I l(l-1) - \epsilon^E(l+1)(l+2)}{\epsilon^I l + \epsilon^E(l+1)} \frac{|a_{l,m_l}|^2}{4\pi R_0^2} \right] + \gamma \left[4\pi R_0^2 + \frac{1}{2} \sum_{l>0,m_l} (l-1)(l+2) |a_{l,m_l}|^2 \right]. \quad (\text{S5})$$

We will show that the $l = 1$ term in Eq. S5 depends on the distance squared of the ion from the droplet COM. In the algebra that follows we will use that

$$\rho^4(\sigma) = R^4 + 4R^3 \sum_{l>0,m_l} a_{l,m_l} Y_{l,m_l}(\sigma) + \dots \quad (\text{S6})$$

In Eq. S6 we keep only the two dominant terms in the summation. The remaining of the terms are neglected because they include powers ≥ 2 of $\delta r = \sum_{l>0,m_l} a_{l,m_l} Y_{l,m_l}(\sigma)$ (δr is a small perturbation relative to R).

We find the coordinates $X_{\text{COM}}, Y_{\text{COM}}, Z_{\text{COM}}$ of the droplet's COM in terms of the expan-

sion coefficients a_{l,m_l} . In the following expressions $d\sigma = \sin\theta d\theta d\phi$.

$$\begin{aligned}
Z_{\text{COM}} &= \frac{1}{V} \int Z(r, \theta, \phi) d^3r = \\
&= \frac{1}{V} \int_{r \leq \rho, \sigma \in S^2} r \cos\theta r^2 d\sigma dr = \\
&= \frac{1}{4V} \int \rho^4(\theta, \phi) \cos\theta d\sigma = \\
&= \frac{1}{V} R^3 \int \cos\theta \sum_{l>0, m_l} a_{l, m_l} Y_{l, m_l}(\sigma) d\sigma = \\
&= \left(\frac{3}{4\pi}\right)^{1/2} a_{1,0}
\end{aligned} \tag{S7}$$

In the fourth line of Eq. S7 we use the orthogonality of the spherical harmonics. Similarly, $X_{\text{COM}} = \Re(a_{1,1})\sqrt{2}$ and $Y_{\text{COM}} = \Im(a_{1,1})\sqrt{2}$.

The $l = 1$ term in Eq. S5 yields

$$\Delta E_1 = \frac{(\epsilon^I - \epsilon^E)Q^2}{8\pi\epsilon^I\epsilon^E R_0} \frac{6\epsilon^E}{\epsilon^I + 2\epsilon^E} \frac{(|a_{1,0}|^2 + |a_{1,1}|^2 + |a_{1,-1}|^2)}{4\pi R_0^2}. \tag{S8}$$

Using Eq. S7 and the similar ones for X_{COM} and Y_{COM} , Eq. S8 becomes

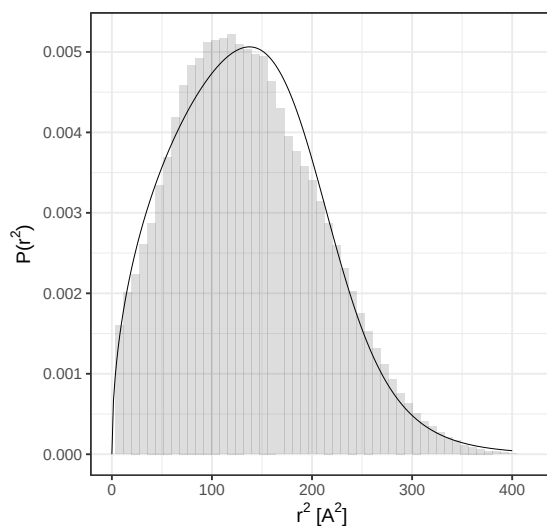
$$\Delta E_1(\|\mathbf{r}\|) = \frac{\epsilon - 1}{4\pi\epsilon_0\epsilon(\epsilon + 2)} \frac{Q^2}{R^3} \|\mathbf{r}\|^2 \tag{S9}$$

where Q , R and ϵ are the charge of the ion, the droplet radius and the relative dielectric constant of the solvent, respectively, ϵ_0 is the vacuum permittivity and $\|\mathbf{r}\|^2 = X_{\text{COM}}^2 + Y_{\text{COM}}^2 + Z_{\text{COM}}^2$. The coefficient in front of $\|\mathbf{r}\|^2$ is denoted as $K(\epsilon)$ and we call it ‘‘spring constant’’. Thus,

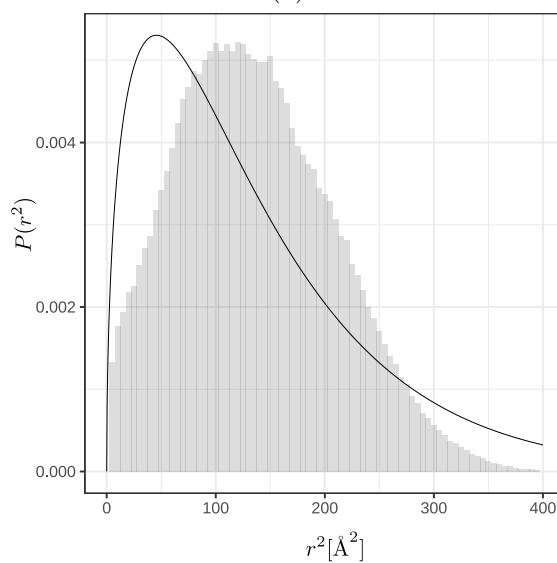
$$K(\epsilon) = \frac{\epsilon - 1}{4\pi\epsilon_0\epsilon(\epsilon + 2)} \frac{Q^2}{R^3}. \tag{S10}$$

The plot of the variation of $K(\epsilon)$ as a function of ϵ is found in the main text.

If the ion is localized in the center of a droplet the Gibbs-Boltzmann distribution of the



(a)



(b)

Figure S1: (a) Distribution of the distances of the sodium ion relative to the COM of the droplet. The equimolar droplet radius is 1.9 nm. The solid line is the product of the logistic and the gamma distribution (with shape parameter 1/2) intended to capture confinement effects. The function is fitted to the distribution using the maximum likelihood estimate (MLE). (b) Same as (a) but the solid line is the gamma function fitted to the distribution using MLE.

ion positions is given by

$$P(\|\mathbf{r}\|^2) = \frac{2}{\sqrt{\pi}} \left(\frac{K(\varepsilon)}{k_B T} \right)^{3/2} \|\mathbf{r}\| e^{-K(\varepsilon)\|\mathbf{r}\|^2/k_B T}. \quad (\text{S11})$$

The expectation value of the square of the distance of the ion from the droplet's COM is given by

$$\langle \|\mathbf{r}\|^2 \rangle = \frac{3}{2} \frac{k_B T}{K(\varepsilon)}. \quad (\text{S12})$$

The conditions under which the EC is more pronounced are discussed in the main text.

We assume that the number density of the solvent in the vicinity of the droplet surface is well approximated by the logistic function (S13)

$$n_{r_0,d}(r) = \frac{1}{1 + \exp(-(r - r_0)/d)} \quad (\text{S13})$$

where d and r_0 are fitting parameters that can be interpreted as the droplet radius and the width of the surface layer. Using the logistic curve for the number density (entropic factor) and gamma function that takes into account the electric potential (energetic factor) we arrive at the following ansatz for the ion distribution

$$p(r^2) \sim r e^{-Kr^2/k_B T} \frac{1}{1 + \exp(-(r - r_0)/d)} \quad (\text{S14})$$

Using the maximum likelihood estimate (MLE) approach we found the most probable parameters $\{K, r_0, d\}$ in order to match the observed values of the distance of the ion from the center of mass. In Fig. S1 we show the fitted and the observed distributions for a single sodium ion in a droplet of 1000 TIP3P (transferable intermolecular potential with three points)^{S5} water molecules. The data were obtained in 15 ns molecular dynamics simulations using the NAMD package.^{S6} The fittings were produced with the use of statistical analysis software R.^{S7} For comparison we contrast the fit that takes into account the surface of the droplet with a fit to a gamma distribution of shape 1/2 in Fig. S1 (b). The analysis

shows that the shape fluctuations of the droplet accounts for the distribution of the ions in the droplet. The fitting can only establish an upper bound of the parameter K . All the variability of the charge distribution is explained by the confinement effect of the droplet surface. In Fig. S1 the fitting parameters used in Eq. (S14) are $r_0 = 14.9\text{\AA}$ and $d = 1.1\text{\AA}$. The effective radius of the droplet is smaller than that of the true molecular surface of water.

Here we demonstrate the effect of geometric vs electrostatic confinement in a droplet composed of 1000 H₂O molecules and a single ion with charge $1e^+$ and $3e^+$. The data are summarized in Table S1.

For a droplet composed of 1000 H₂O molecules (equimolar radius = 1.93 nm) and a $1e^+$ ion, if we assume $\varepsilon = 80$ at $T = 300$ K then Eq. S10 yields $K = 0.39$ [mJ/m²] and Eq. S12 yields $\langle\|\mathbf{r}\|^2\rangle = 16$ [nm²]. The simulations for the same system yield $\langle\|\mathbf{r}\|^2\rangle = 1.36$ [nm²]. These data are shown in the first line of Table S1. The fact that the estimated value of $\langle\|\mathbf{r}\|^2\rangle$ is larger than the droplet's radius squared implies that the geometric confinement dominates over the electrostatic confinement.

In the second line of Table S1, we use the $\langle\|\mathbf{r}\|^2\rangle = 1.36$ [nm²] (from simulations) and the data are fitted with a gamma distribution to yield K . In the third line of Table S1, the same data are fitted with Eq. S14, which yields an upper bound for K .

In the fourth and fifth lines of Table S1, we show data for a droplet composed of 1000 H₂O molecules and a $3e^+$ ion. The fitting with a gamma distribution of the simulation data yields $K = 20.7$ [mJ/m²]. This value of K yields $\varepsilon = 38$. In the fifth line, we estimate the value of K from Eq. S12, where $\langle\|\mathbf{r}\|^2\rangle$ is the value estimated from the simulations. Thus, estimation of K by two independent ways yield very similar. The similarity indicates that the electrostatic confinement becomes significant for this system.

The estimated values of the dielectric constant ($\varepsilon = 38$) is lower than the typical values of the pure solvent. We believe that the apparent decrease in the dielectric constant is connected with the polarization saturation in the vicinity of the charge ion.

Table S1: Values of the parameter K for selected simulations of an ion in a droplet. All the estimates are at $T = 300$ K. Details are presented in the text.

	Size [N]	Charge [Q]	K [mJ/m ²]	$\langle \ \mathbf{r}\ ^2 \rangle$ [nm ²]
Theor. $\epsilon = 80$	1000	1 e ⁺	0.39	15.3
Sim. Gamma	1000	1 e ⁺	4.53	1.36
Sim. Confinement	1000	1 e ⁺	< 0.83	1.36
Sim. Gamma	1000	3 e ⁺	20.7	0.30
Theor. $\epsilon = 38$	1000	3 e ⁺	20.5	0.30

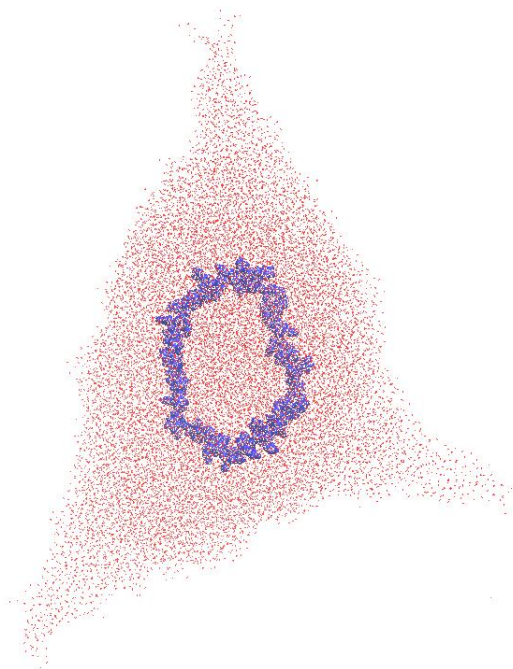


Figure S2: Snapshots of aqueous droplets with a charged cyclic peptide. Spikes formed when the charge squared-to-volume ratio is above a certain threshold value defined by the Rayleigh limit.

The results of the simulations of a sodium ion in water droplet can be compared with the results of the simulations of a cyclic peptide in Fig. 2 in the main text.

S2. Models and simulation methods

Table S2: Simulation parameters. N denotes the number of H_2O molecules in the simulation box of dimension L . N_d is the average number of the H_2O molecules that form a connected drop, τ is an upper bound on the relaxation time and t_{run} is the duration of the run. The “*” superscript in the temperature refers to simulations started with Na^+ ion(s) in or near the droplet center. R_e denotes the equimolar radius.

N (H_2O)	L (nm)	T (K)	N_{Na}	t_{run} (μs)	N_d	R_e (nm)	τ (ns)
100	10	200	1	1.6	100	0.87	0.4
		260	1	1.6	99.8		0.8
200	10	200	1	1.6	200	1.10	0.8
		260	1	1.6		199.8	0.8
360	10	200	1	1.6	360	1.35	0.4
		200*	1	0.44	360	1.35	0.4
		300	1	1.6	359.3	1.35	0.2
776	15	200	1	0.33	776	1.77	0.8
		200*	1	0.46	776	1.77	0.8
		200*	5	0.53	776	1.77	0.8
		300	1	0.77	773.9	1.75	0.4
1100	20	200	1	0.32	1100	2.0	1.6
		200*	8	0.055	1100	2.0	1.6
		300	1	0.32	1095.1	1.97	0.8

A. Simulations of aqueous nanodroplets with Na^+ ions We simulate Na^+ ions in aqueous nanodroplets at $T = 200$ K, 260 K, and 300 K, representing the room temperature and supercooled conditions. The system sizes and length of simulations are shown in Table S2. The simulations were performed by molecular dynamics (MD) as implemented in GROMACS v4.6.1.^{S11–S14} The water molecules were modeled with the TIP4P/2005 (transferable intermolecular potential with four points) model.^{S15} The Na^+ parameters are shown in Table S3. The interactions of the ion with the O site of the water molecules are calculated with the combining rules $\epsilon_{\text{Na},\text{O}} = \sqrt{\epsilon_{\text{Na}}\epsilon_{\text{O}}}$ and $\sigma_{\text{Na},\text{O}} = \sqrt{\sigma_{\text{Na}}\sigma_{\text{O}}}$.

Each nanodroplet has been placed in a periodic cubic box of length L (see Table S2). The box is large enough to avoid any interaction between the water droplet and its periodic

Table S3: Charge and Lennard-Jones (LJ) parameters (σ_{LJ} representing the atomic diameter and ϵ_{LJ} , depth of the potential energy minimum) for the ions used with the TIP4P/2005 water model.

Ion	Charge (e)	ϵ_{LJ} (kJ/mol)	σ_{LJ} (nm)
Na ⁺ (Ref. ^{S8})	+1	0.0115980	0.333045
Li ⁺ (Ref. ^{S8})	+1	0.0764793	0.212645
Cs ⁺ (Ref. ^{S8})	+1	0.000338904	0.671600
F ⁻ (Ref. ^{S9})	-1	3.01248	0.273295
Cl ⁻ (Ref. ^{S9})	-1	0.492833	0.441724
I ⁻ (Ref. ^{S10})	-1	0.292880	0.540000

images. The length of cutoff for interactions (Coulomb and Lennard-Jones) is at $L/2$, which is much larger than the droplet’s diameter in order to reproduce long range electrostatic interactions within the droplet. The temperature was controlled with the Nosé-Hoover thermostat with time constant 0.1 ps. The equations of motion are integrated with the leap-frog algorithm with a time step of 2 fs.

The simulations were initiated with a condensed pure water nanodroplet where the Na⁺ ion were placed at the surface for the majority of the single Na⁺ runs, and in the center for two runs, $N = 360$ and 776 at $T = 200$ K. All runs with multiple Na⁺ ions start with the ions near the droplet center of mass.

In Table S2, the mean number of molecule, N_d , forming the connected cluster (i.e. those not in the vapor), and the relaxation time τ , determined from the neighbor correlation function are shown.^{S16} The values of τ provide an estimate for the relaxation time for simulations that include ions. In the temperature range where simulations are performed the solvent evaporation within the simulation box is negligible.

To ensure that we sufficiently sample an equilibrated system after the addition of a single Na⁺ ion at 200 K, where the concern for equilibration is the highest, we run two simulations for each of $N = 360$ and $N = 776$ nanodroplets. In one set, we set the Na⁺ ion at or near the centre of the droplet, quench the system through a conjugate-gradient energy minimization, and then proceed with an MD simulation. In the other, we initially place the ion on the surface. Equilibration time is estimated from the time it takes for the results of

the simulations from the two different conditions to converge. For example, for $N = 776$ after 400 ns, the ion densities as a function of radial distance from the droplet COM $\rho_{\text{Na}}(r)$ converge for the two simulations. For $N = 1100$, we assume that the equilibration time is longer by a factor of $\tau_{1100}/\tau_{776} \approx 2$. For multiple ions, initially distributed in the nanodroplet interior, we presume that the relaxation time is shorter and that the single ions simulations provide upper bounds on the relaxation times.

B. Simulations of aqueous nanodroplets with Li^+ , Cs^+ and anions We performed MD simulations of droplets comprised 100 and 776 H_2O molecules and a single F^- , Cl^- , I^- , Li^+ , Cs^+ ion. The simulations were performed with NAMD 2.14.^{S6} The water molecules were modeled with the TIP4P/2005 model.^{S15} The ion Lennard-Jones parameters are shown in Table S3.

The Newton’s equation of motion for each atomic site was integrated using the velocity-Verlet algorithm with a time step of 2.0 fs. All the forces were computed directly without any cut-offs. Equilibrium simulations in NAMD were set by placing the droplet in a spherical cavity of radius 20.0 nm by using spherical boundary condition. The systems were thermalized with the Langevin thermostat with the damping coefficient set to 1/ps. The simulation included a 0.2 μs equilibration period followed by a 1.0 μs production run, with configurations sampled every 0.1 ns. At 200 K two simulations started with the ion placed initially near the COM and on the surface.

C. Simulations of aqueous nanodroplets with polarizable force field We performed MD simulations of droplets comprised 880 H_2O molecules and a single Na^+ and Li^+ ion at 350 K and 200 K. The simulations were performed by using the software NAMD version 2.14.^{S6} The water molecules were modeled with the SWM4-NDP model^{S17} and the ions were modelled with the CHARMM Drude force field.^{S18,S19} The SWM4-NDP model is a 5-site model with four charge sites and a negatively charged Drude particle connected to the oxygen atom, while the ions are modeled with one charge site and a negatively charged

Drude particle. Hereafter, we will refer to the SWM4-NDP model as SWM4 for brevity. A dual Langevin thermostat was utilized to freeze the Drude oscillators while maintaining the warm degrees of freedom at the desired temperature.^{S20} The systems were thermalized with Langevin thermostat at 350 K (for the warm degrees of freedom) and at 1 K for the Drude oscillators. The damping coefficient for the Langevin thermostat was set to 1/ps. The length of the production run was 100 ns, sampled every 0.5 ps for high temperature runs and every 100 ps for low temperature runs. The simulation protocol was the same as for the ions in S2.B.

S3. Water density and structure, and single Na^+ radial concentration for various droplet sizes

Table S4: Number density based on the number of oxygen sites in the core ($0 < r < R_B$) and subsurface ($R_B < r < R_V$). The error in the densities is ± 0.15 .

Ion	N, T (K)	number density (nm^{-3}) at $0 < r < R_B$	number density (nm^{-3}) at $R_B < r < R_V$
Na^+	776, 200 K	33.66	34.56
	776, 300 K	34.38	34.14
	1100, 200 K	33.08	34.11
	1100, 300 K	34.26	34.03
F^-	776, 200 K	33.71	34.60
Cl^-	776, 200 K	33.37	34.40
	776, 300 K	34.13	33.98

Figure S3 shows $\rho(r)$ and $\rho_V(r)$ for pure water nanodroplets of all sizes studied at high (300 K for $N \geq 200$, 260 K for $N \leq 200$) and low (200 K) temperature (T), with data taken from Ref.^{S16} At high T , shown in Fig. S3 (a), $\rho(r)$ is that of a typical liquid droplet, characterized by a flat (slowly decreasing) curve in the interior that decays sigmoidally to (near) zero over approximately an intermolecular distance at the liquid-vapor interface. The exceptions are the curves for $N \leq 200$, that at 260 K show some ordering or layering particularly near the surface. At low T , shown in Fig. S3 (b), there are significant undulations in the density profiles for all nanodroplet sizes, and, as seen particularly well for the larger nanodroplets, an increase in density as r increases towards the surface.

The undulations in $\rho(r)$ make it difficult to characterize how the local density changes with r , and for this reason we plot $\rho_V(r)$. Fig. S3 (c) shows $\rho_V(r)$ monotonically decreasing (or flat) with r for all nanodroplet sizes at high T . $\rho_V(r)$ is significantly smoother than $\rho(r)$, as it does not depend on the number density itself, but rather on the Voronoi volume surrounding each water molecule. An important feature of $\rho_V(r)$ is that it begins to decay to zero at approximately 0.3 nm, or an intermolecular distance, before $\rho(r)$; Voronoi volumes are very large, and Voronoi-based density very low, for molecules on the surface. Molecules

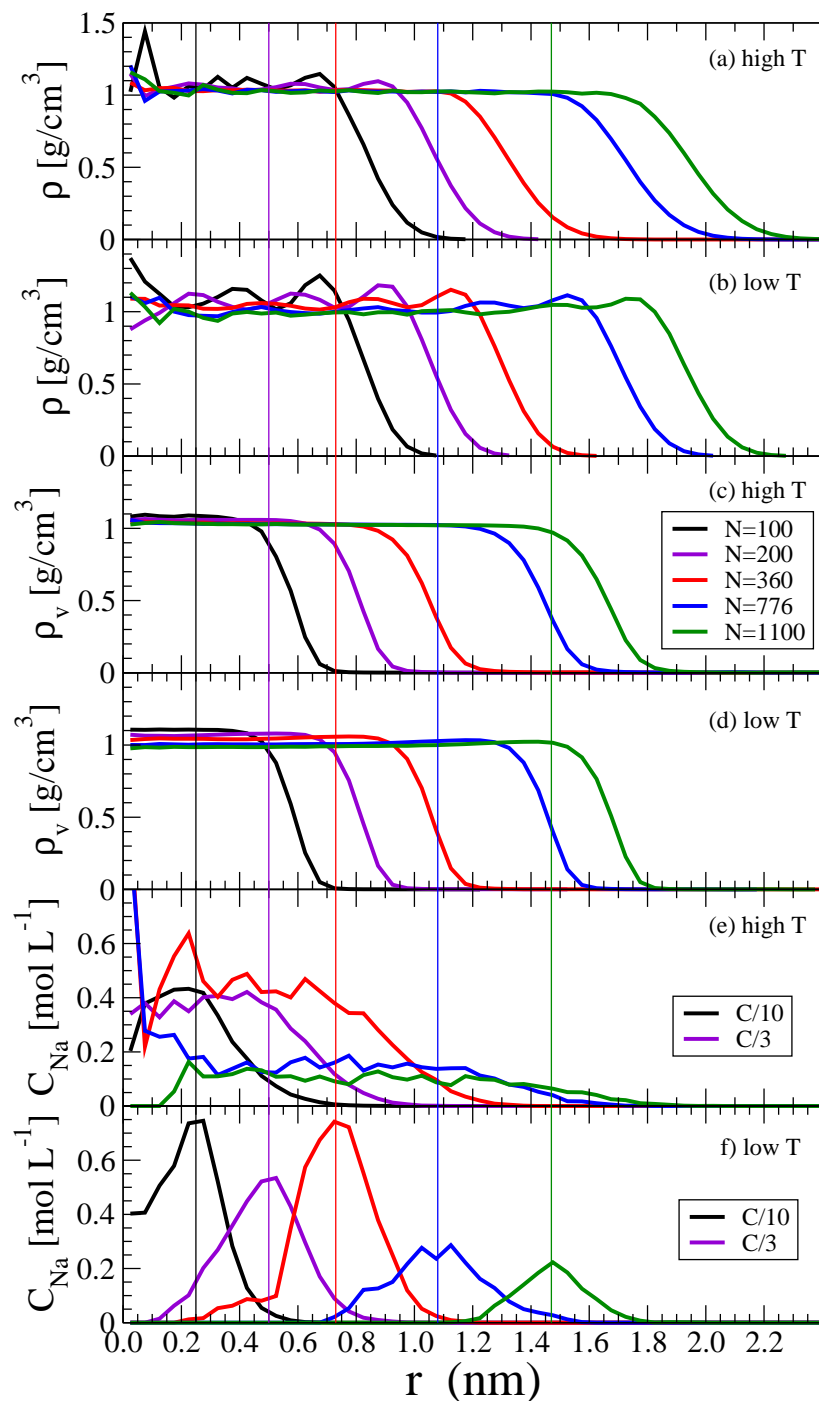


Figure S3: Pristine water nanodroplet structure and single Na number density distributions for low temperature ($T = 200$ K) and high temperatures ($T = 260$ K for $N \leq 200$ and $T = 300$ K for $N \geq 360$). Panels (a) and (b) show water density $\rho(r)$; panels (c) and (d) show water density based on molecular Voronoi volumes $\rho_V(r)$. Panels (e) and (f) show Na^+ concentration $C_{\text{Na}}(r)$, which for $N = 100$ and $N = 200$ have been reduced by a factor of 10 and 3, respectively.

falling within the range where $\rho_V(r)$ is high (near bulk values) are completely surrounded by other water molecules and are not on the surface. Surface molecules can be identified as those located where $\rho_V(r)$ is small, and molecules in the subsurface as those located an intermolecular distance below the point at which $\rho_V(r)$ has decayed to near zero.

Fig. S3 (d) shows $\rho_V(r)$ for nanodroplets at low T . For $N \geq 200$, there is a significant increase in density in the subsurface layer. The density may well be higher for surface molecules, but $\rho_V(r)$ can not characterize this. This increased density at low T appears to be a hallmark of cold water nanodroplets, and has not been reported for simple liquids to our knowledge. It is this heterogeneous environment in pure water that lends an interesting backdrop for studying ion distributions at low T .

In Fig. S3 (e), we plot $C_{\text{Na}}(r)$ at high T for systems composed of a single Na^+ ion within a nanodroplet. Since the ion density is quite high for small nanodroplets, we divide $C_{\text{Na}}(r)$ by 10 and 3 for $N = 100$ and 200, respectively. In all cases, the $C_{\text{Na}}(r)$ is approximately constant in the interior of the droplet, and begins to decay within the subsurface, and decays to zero significantly before $\rho(r)$ does.

Fig. S3 (f) shows a dramatic difference in $C_{\text{Na}}(r)$ at low T . Rather than being centered at $r = 0$, the peak of $C_{\text{Na}}(r)$ is located within 0.1 nm of the peak in $\rho_V(r)$ (for $N \geq 200$). Thus, we see that in a nanodroplet with a heterogeneous radial density, as determined by $\rho_V(r)$, the single Na^+ ion tends to reside in the highest density environment.

For $N = 100$ at low T , $\rho_V(r)$ is approximately constant for $r < 0.3$ nm, and then decreases with increasing r . While a constant $C_V(r)$ for $r < 0.3$ nm suggests that $C_{\text{Na}}(r)$ should be uniform in this interior region, we see that $C_{\text{Na}}(r)$ is in fact peaked just below 0.3 nm. We do see, however, that the peak in $C_{\text{Na}}(r)$ coincides with a local minimum in $\rho(r)$, suggesting that layering may play a significant role in determining where the Na ion resides in such small nanodroplets.

In Fig. S4, we plot for 200 K $\rho(r)$, $C_{\text{Na}}(r)$ for a single Na ion, $q_T(r)$ and $d_5(r)$, confirming that for $N = 360, 776$, and 1100, the ion resides in a subsurface that is relatively disordered

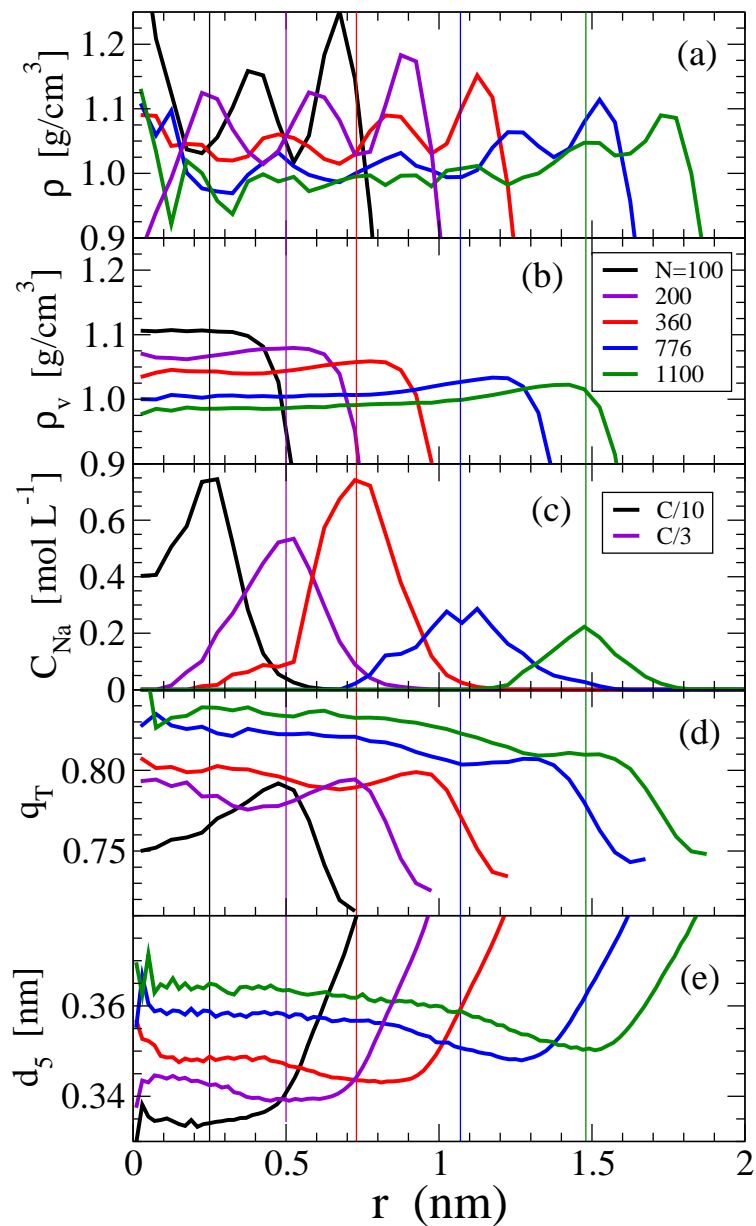


Figure S4: Single Na^+ concentration and measures of structure for low temperature ($T = 200$ K) for nanodroplet sizes $N = 100$ (black), 200 (violet), 360 (red), 776 (blue) and 1100 (green). Shown are (a) ρ , (b) ρ_v , (c) C_{Na} , (d) q_T and (e) d_5 , as functions of r . ρ , ρ_v , q_T and d_5 are for pure water.

compared to the tetrahedral core. Data for $q_T(r)$ and $d_5(r)$ are taken from Ref.^{S21} $C_{\text{Na}}(r)$ decays rapidly for increasing r upon approaching the surface layer (where $d_5(r)$ rapidly increases) and for decreasing r upon entering the region where $q_T(r)$ is high. The exception is the $N = 100$ nanodroplet, which does not have a tetrahedral core. At this size, however, layering propagating from the surface extends to the droplet interior, and it is at a minimum in $\rho(r)$ that we find the peak in $C_{\text{Na}}(r)$. For the larger droplets too, it appears that the ion prefers to be in a trough, except for $N = 1100$, where layering is relatively weak.

S4. Convergence of the ion location and comparison of the radial probability density of various ions in a 776- H_2O -molecule droplet

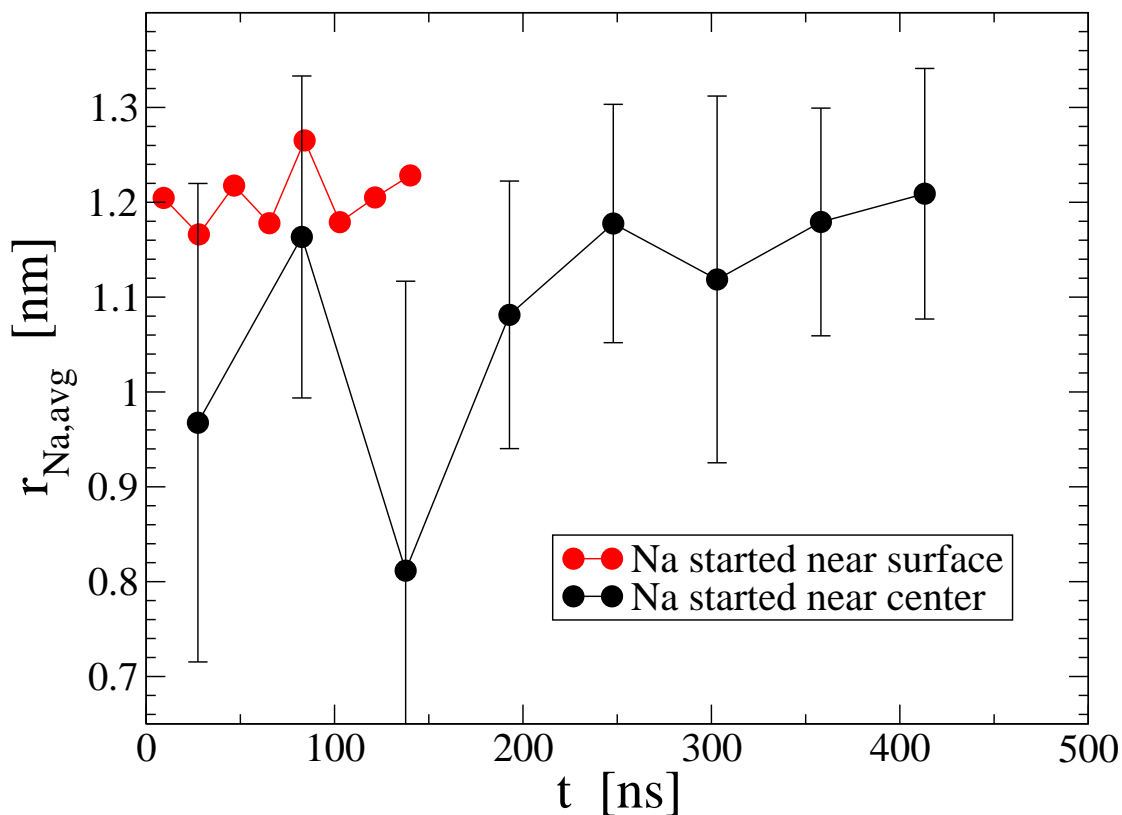


Figure S5: Average radial position of ion as a function of time in a system of a single Na^+ ion and $N = 776$ at $T = 200$ K. Each time series is divided into eight equal blocks over which averages are reported. Bars for the case where Na^+ starts at the surface represent one standard deviation. $R_B = 0.73$ nm, $R_V = 1.49$ nm and $R_e = 1.77$ nm for this case.

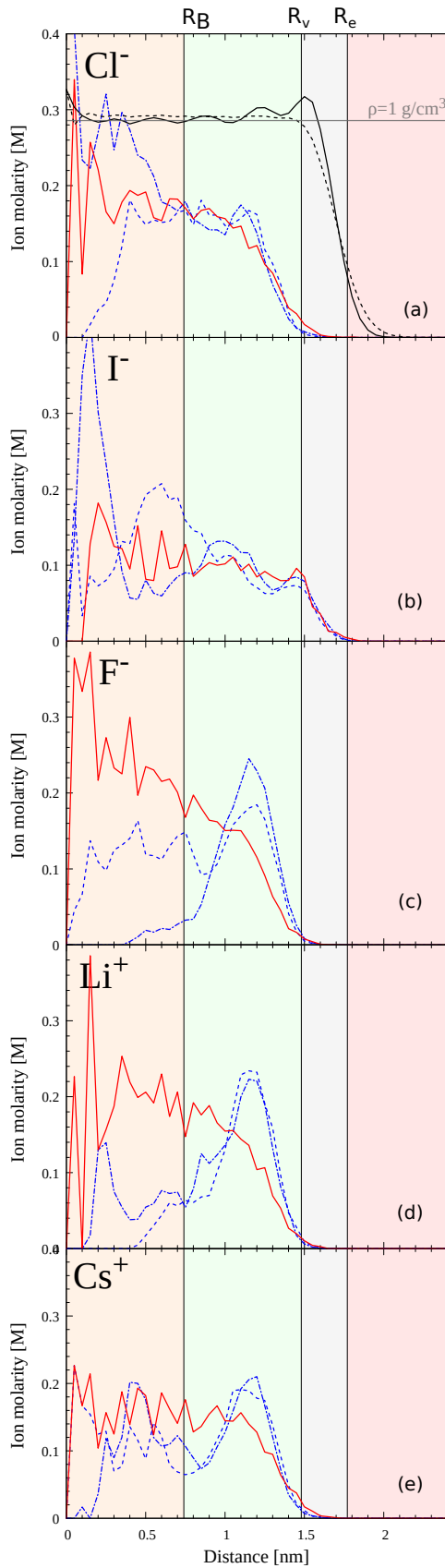


Figure S6: Concentration profiles for various ions. Red line at 300 K, blue S-19 lines at 200 K.

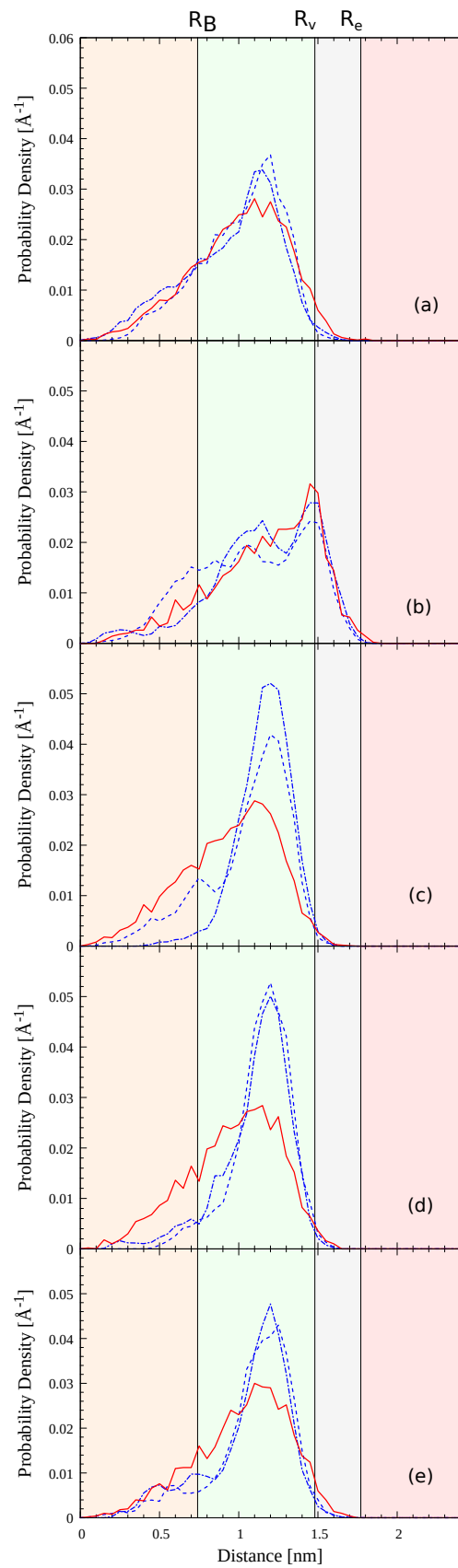


Figure S7: Same as Fig. S7 but with no volume normalization.

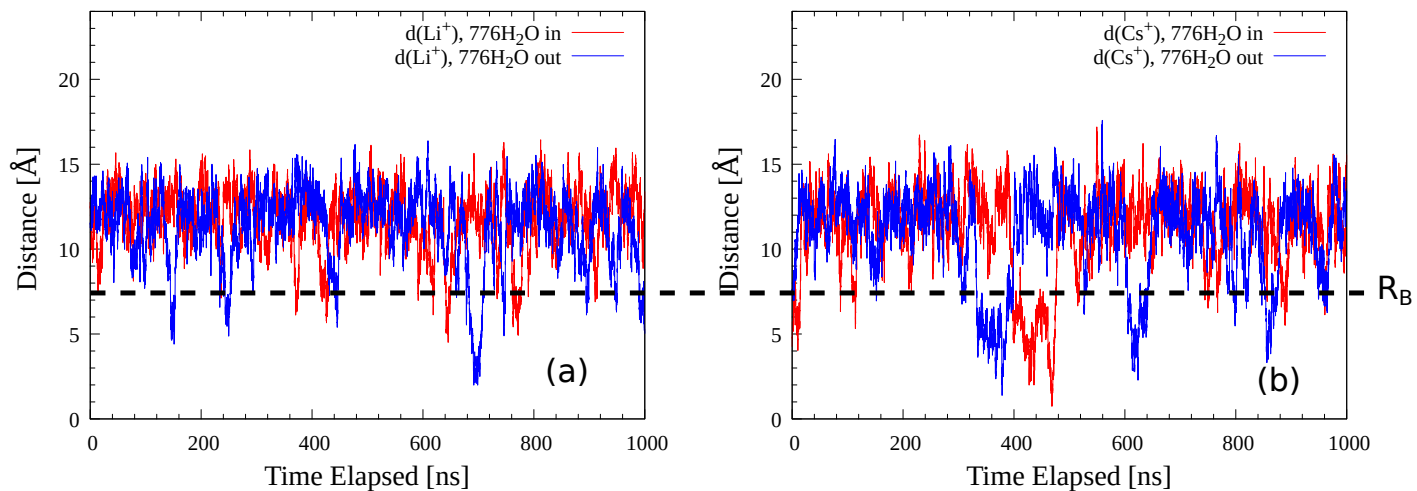


Figure S8: Time evolution of the ion, Cs^+ and Li^+ , distance from the droplet COM. The two lines (blue and red) correspond to the different MD trajectories starting from the droplet center and surface. The data presented here and analyzed in Figs. S6 and S7 are those following 200 ns of initial equilibration time.

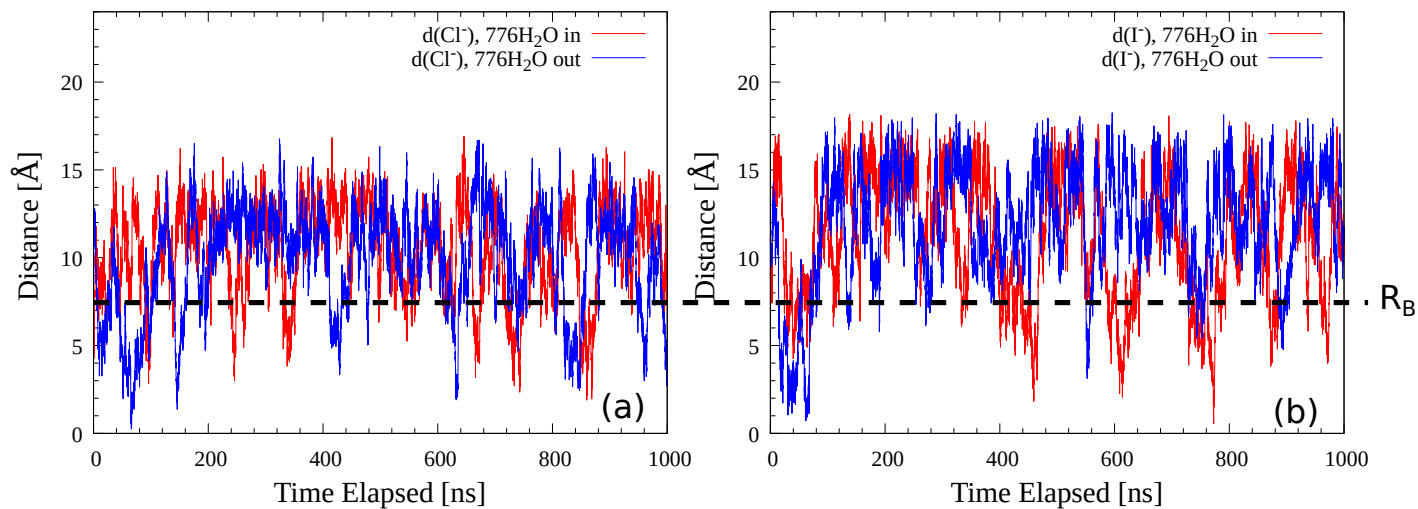


Figure S9: Same as Fig. S8 but for Cl^- and I^- .

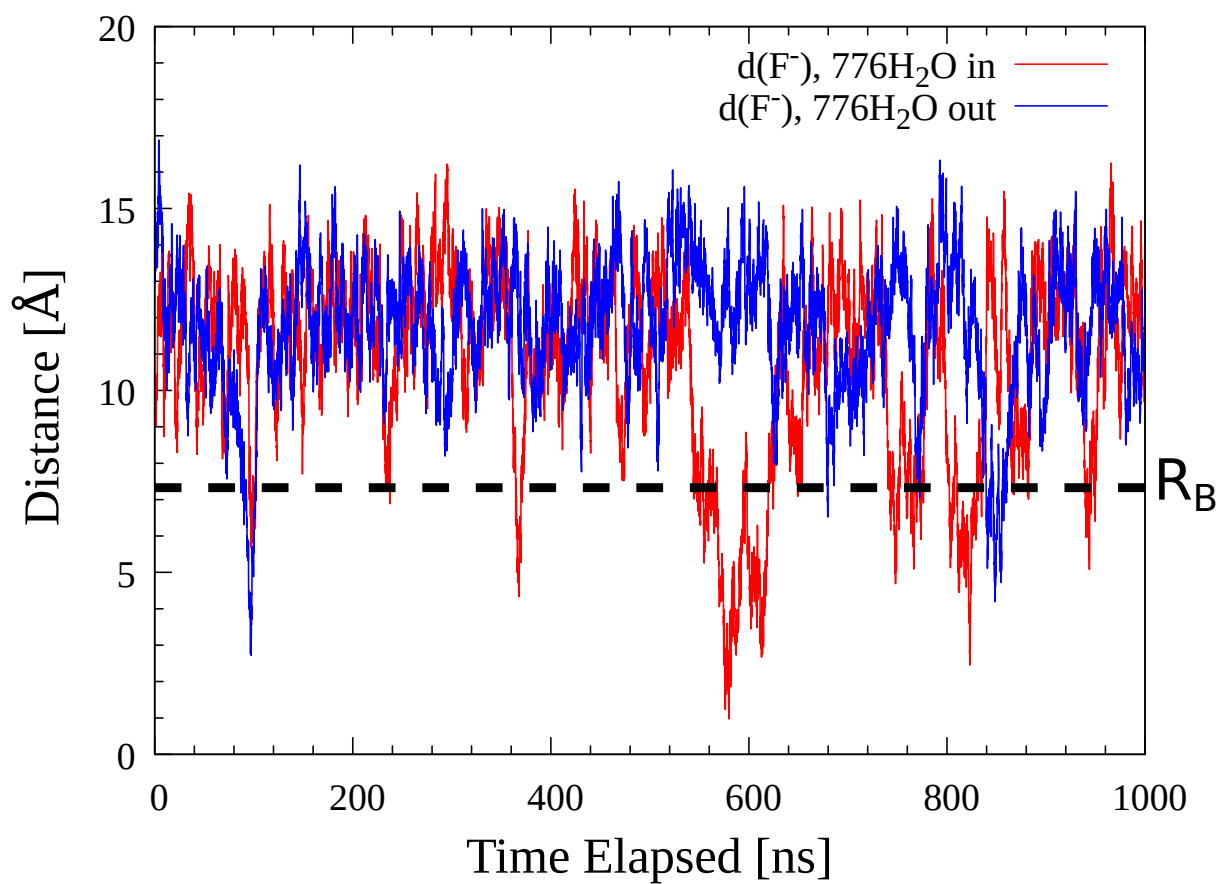


Figure S10: Same as Fig. S8 but for F^- .

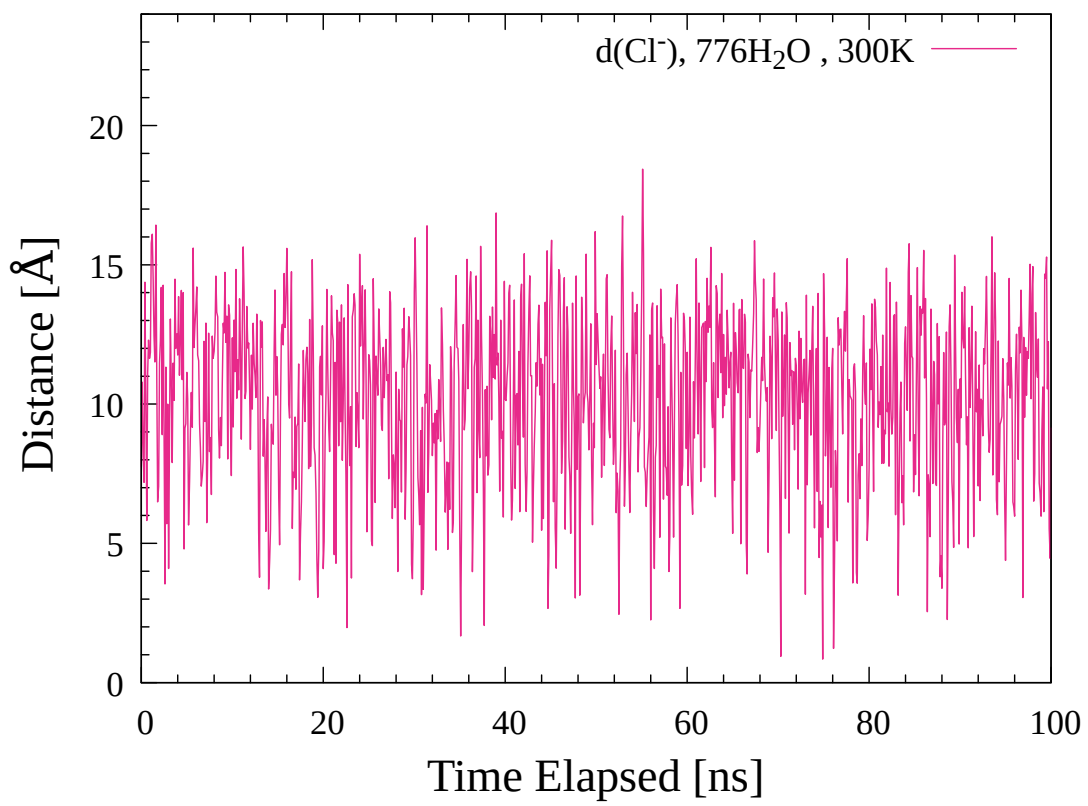
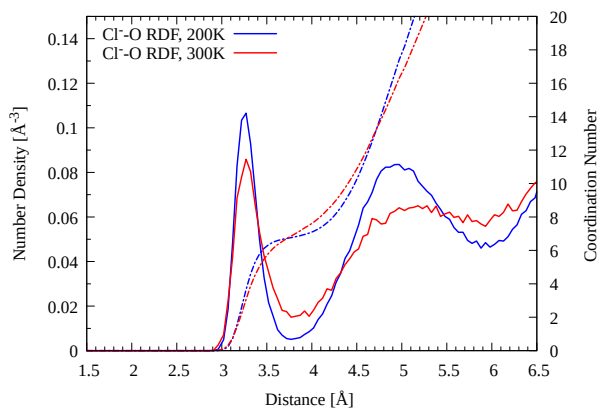
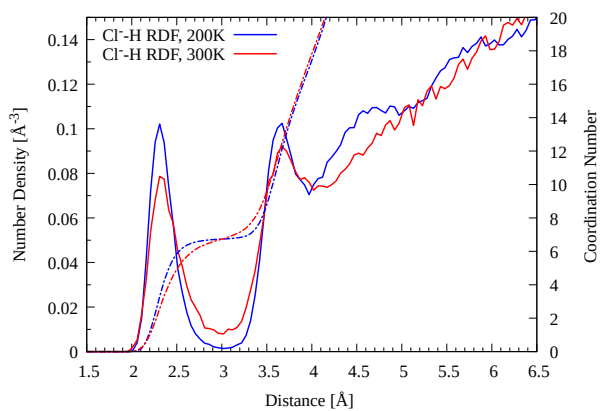


Figure S11: Same as Fig. S8 but for Cl⁻ at 300 K.

S5. Cl^- and F^- radial distribution functions in a 776- H_2O -molecule droplet

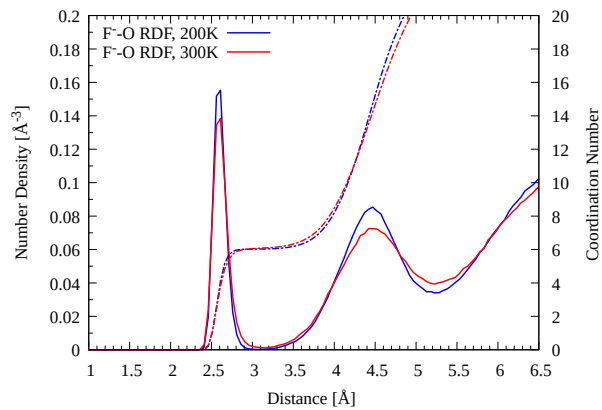


(a)

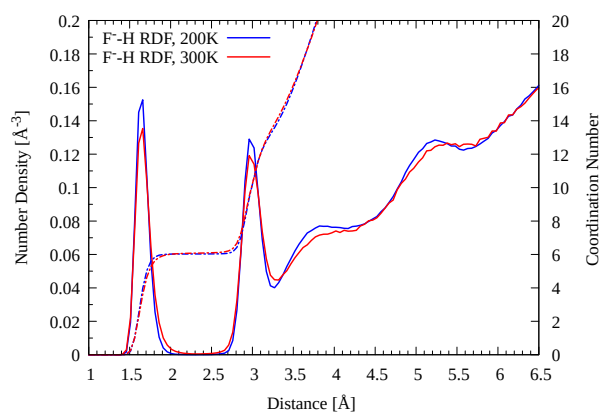


(b)

Figure S12: Radial distribution function ($g(r)$) at 200 K and 300 K for (a) O-Cl and (b) H-Cl.



(a)



(b)

Figure S13: Radial distribution function ($g(r)$) at 200 K and 300 K for (a) O-F and (b) H-F.

S6. Radial distributions of ions using polarizable force field

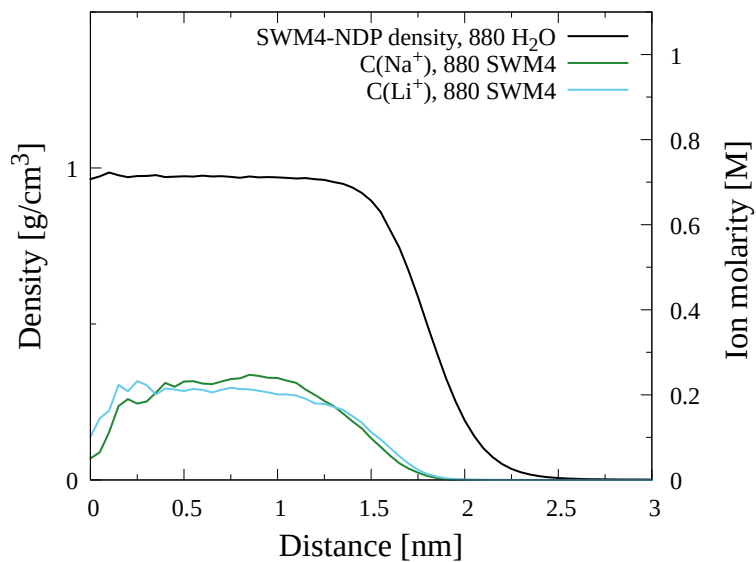


Figure S14: Concentration profiles of Li^+ and Na^+ ions (measured in the right y-axis) and water density (measured in the left y-axis) in a droplet comprising 880 H_2O molecules at $T = 350$ K.

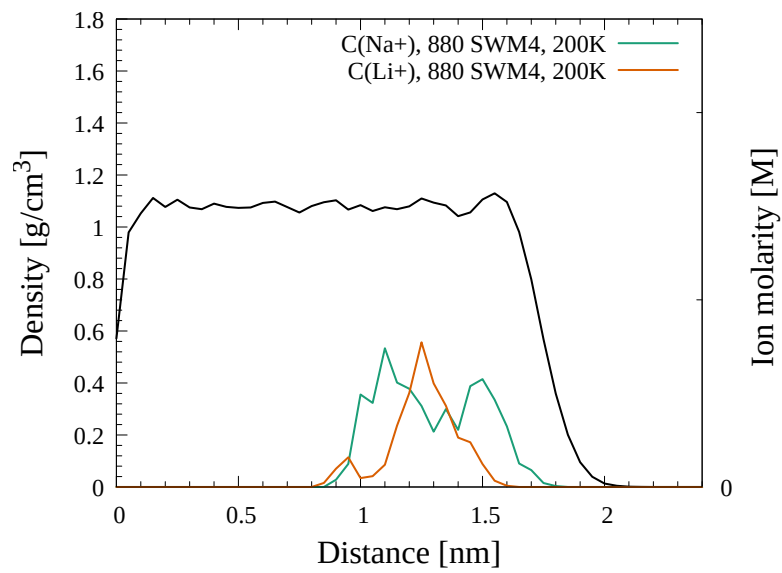


Figure S15: Same as Fig. S14 but at $T = 200$ K.

S7. Radial distribution of multiple Na^+ ions in a droplet of 776 H_2O molecules

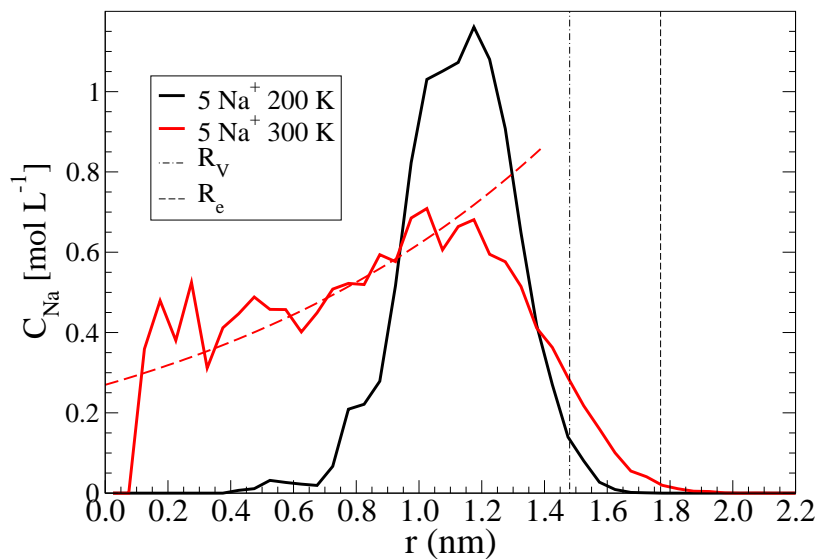


Figure S16: $C_{\text{Na}}(r)$ for the 776-molecule droplet with 5 Na^+ ions. Red dashed curve indicates a fit to Eq. ?? (main text). The distribution at 300 K decays (toward the droplet's COM) as an exponential function fitted by $0.42 \exp(-(1.14 - r)/1.2) \times 10/6.022$, where $\lambda_{\text{PB}} \approx 1.2$ nm. The vertical lines mark R_V and R_e .

References

- (S1) Consta, S.; Malevanets, A. Disintegration mechanisms of charged nanodroplets: novel systems for applying methods of activated processes. *Mol. Simul.* **2015**, *41*, 73–85.
- (S2) Oh, M. I.; Malevanets, A.; Paliy, M.; Frenkel, D.; Consta, S. When droplets become stars: charged dielectric droplets beyond the Rayleigh limit. *Soft Matter* **2017**, *13*, 8781–8795.
- (S3) Rayleigh, L. XX. On the equilibrium of liquid conducting masses charged with electricity. *Philos. Mag.* **1882**, *14*, 184–186.
- (S4) Jackson, J. D. *Classical Electrodynamics*, third ed. ed.; John Wiley & Sons: New York, NY, 1998.
- (S5) Jorgensen, W. L.; Jenson, C. Temperature dependence of TIP3P, SPC, and TIP4P water from NPT Monte Carlo simulations: Seeking temperatures of maximum density. *J. Comput. Chem.* **1998**, *19*, 1179–1186.
- (S6) Phillips, J. C.; Braun, R.; Wang, W.; Gumbart, J.; Tajkhorshid, E.; Villa, E.; Chipot, C.; Skeel, R. D.; Kalé, L.; Schulten, K. Scalable molecular dynamics with NAMD. *J. Comput. Chem.* **2005**, *26*, 1781–1802.
- (S7) R Core Team, R: A Language and Environment for Statistical Computing. R Foundation for Statistical Computing: Vienna, Austria, 2017.
- (S8) Aqvist, J. Ion-water interaction potentials derived from free energy perturbation simulations. *J. Phys. Chem.* **1990**, *94*, 8021–8024.
- (S9) Chandrasekhar, J.; Spellmeyer, D. C.; Jorgensen, W. L. Energy component analysis for dilute aqueous solutions of lithium(1+), sodium(1+), fluoride(1-), and chloride(1-) ions. *J. Am. Chem. Soc.* **1984**, *106*, 903–910.

- (S10) McDonald, N. A.; Duffy, E. M.; Jorgensen, W. L. Monte Carlo Investigations of Selective Anion Complexation by a Bis(phenylurea) p-tert-Butylcalix[4]arene. *J. Am. Chem. Soc.* **1998**, *120*, 5104–5111.
- (S11) Berendsen, H. J. C.; van der Spoel, D.; van Druren, R. GROMACS: A message-passing parallel molecular dynamics implementation. *Comput. Phys. Commun.* **1995**, *91*, 43.
- (S12) Lindahl, E.; Hess, B.; van der Spoel, D. GROMACS 3.0: A package for molecular simulation and trajectory analysis. *J. Mol. Model.* **2001**, *7*, 306.
- (S13) van der Spoel, D.; Lindahl, E.; Hess, B.; Groenhof, G.; Mark, A. E.; Berendsen, H. J. C. GROMACS: Fast, Flexible and Free. *J. Comput. Chem.* **2005**, *26*, 1701.
- (S14) Hess, B.; Kutzner, C.; van der Spoel, D.; Lindahl, E. GROMACS 4: Algorithms for highly efficient, load balanced, and scalable molecular simulation. *J. Chem. Theory Comput.* **2008**, *4*, 435.
- (S15) Abascal, J. L. F.; Vega, C. A general purpose model for the condensed phases of water: TIP4P/2005. *J. Chem. Phys.* **2005**, *123*, 234505.
- (S16) Malek, S. M. A.; Poole, P. H.; Saika-Voivod, I. Thermodynamic and structural anomalies of water nanodroplets. *Nat. Commun.* **2018**, *9*, 2402.
- (S17) Lamoureux, G.; Harder, E.; Vorobyov, I. V.; Roux, B.; MacKerell, A. D. A polarizable model of water for molecular dynamics simulations of biomolecules. *Chem. Phys. Lett.* **2006**, *418*, 245–249.
- (S18) Yu, H.; Whitfield, T. W.; Harder, E.; Lamoureux, G.; Vorobyov, I.; Anisimov, V. M.; MacKerell, A. D.; Roux, B. Simulating Monovalent and Divalent Ions in Aqueous Solution Using a Drude Polarizable Force Field. *J. Chem. Theory Comput.* **2010**, *6*, 774–786, PMID: 20300554.

- (S19) Luo, Y.; Jiang, W.; Yu, H.; MacKerell, A. D.; Roux, B. Simulation study of ion pairing in concentrated aqueous salt solutions with a polarizable force field. *Faraday Discuss.* **2013**, *160*, 135–149.
- (S20) Jiang, W.; Hardy, D. J.; Phillips, J. C.; MacKerell, A. D.; Schulten, K.; Roux, B. High-Performance Scalable Molecular Dynamics Simulations of a Polarizable Force Field Based on Classical Drude Oscillators in NAMD. *J. Phys. Chem. Lett.* **2011**, *2*, 87–92, PMID: 21572567.
- (S21) Malek, S. M. A.; Poole, P. H.; Saika-Voivod, I. Surface tension of supercooled water nanodroplets from computer simulations. *J. Chem. Phys.* **2019**, *150*, 234507.

Low density interior in supercooled aqueous nanodroplets expels ions to the subsurface

Shahrazad M. A. Malek,[†] Victor Kwan,[‡] Ivan Saika-Voivod,^{†,¶} and Styliani Consta^{*,‡}

[†] *Department of Physics and Physical Oceanography, Memorial University of Newfoundland, Canada, A1B 3X7*

[‡] *Department of Chemistry, The University of Western Ontario, London, Ontario, Canada N6A 5B7*

[¶] *Department of Applied Mathematics, Western University, London, Ontario, Canada, N6A 3K7*

E-mail: sconstas@uwo.ca

Abstract

The interaction between water and ions within droplets plays a key role in the chemical reactivity of atmospheric and man-made aerosols. Here we report direct computational evidence that in supercooled aqueous nanodroplets a lower density core of tetrahedrally coordinated water expels the cosmotropic ions to the denser and more disordered subsurface. In contrast, at room temperature, depending on the nature of the ion the radial distribution in the droplet core is nearly uniform or elevated towards the center. We analyze the spatial distribution of a single ion in terms of a reference electrostatic model. The energy of the system in the analytical model is expressed as the sum of the electrostatic and surface energy of a deformable droplet. The model predicts that the ion is subject to a harmonic potential centered at the droplet's center of mass. We name this effect "electrostatic confinement". The model's predictions are consistent with the simulation findings for a single ion at room temperature but not at supercooling. We anticipate this study to be the starting point for investigating the structure of supercooled (electro)sprayed droplets that are used to preserve the conformations of macromolecules originating from the bulk solu-

tion.

Introduction

The spatial distribution of ions in droplets plays a decisive role in chemical reactivity in atmospheric and man-made aerosols. Applications of the man-made aerosols relevant to this study include spray-based ionization methods used in native mass spectrometry analysis¹ and use of droplets as micro- (nano-) reactors for accelerating chemical synthesis.²⁻⁴ Aerosol droplets in the lower atmosphere carry a small charge determined by at most a few excess ions whereas droplets in thunderclouds and (electro)sprays are highly charged. In this article we show how a heterogeneous solvent structure in supercooled aqueous mesoscopic clusters charged with ions changes their spatial distribution relative to that at room temperature. Hereafter, we will use the term nanodroplets for these mesoscopic clusters.

The structure and stability of supercooled clusters composed of ionic species has fascinated scientists over several decades. Most of the experiments have been performed for clusters composed of a few tens of water molecules. Experiments have detected abun-

dance of certain “magic” cluster sizes associated with clathrate structures⁵ and have studied their reactivity in atmospheric chemistry.⁶ Many of these experiments have used Fourier transform ion cyclotron resonance (FT-ICR) mass spectrometry where dominant evaporative cooling of clusters over heating due to the absorption of black body radiation from the warmer walls of the apparatus^{5,6} has been reported. In certain FT-ICR experiments the temperature of clusters composed of 50-70H₂O molecules is estimated to be 130 K-150 K. The hydration of ions in clusters at supercooling and elevated temperature in the last decade is actively investigated using infrared photodissociation spectroscopy.⁷⁻⁹ Moreover, supercooled droplets are used to preserve peptide conformations originating from the bulk solution in ion mobility and mass spectrometry experiments.¹

Most of the computational studies^{10-12,12-16,16-20,20-30} are for clusters at room or elevated temperature, while there are relatively few computational studies^{15,17} of the supercooled clusters due to fact that they are notoriously challenging to be equilibrated. Voth and co-workers¹⁷ have investigated the location of a single Na⁺, Cl⁻ and H₃O⁺ ion in clusters of up to 100 H₂O molecules in the temperature range of 100 K-450 K. They found that in supercooled clusters of 100 H₂O molecules H₃O⁺ and Na⁺ tend to reside within a few monolayers of the surface. At room and elevated temperature both the Na⁺ and Cl⁻ ions are found nearer to the center, while the H₃O⁺ continues to be near the surface.

The spatial distribution of multiple ions in nanodroplets has been investigated less.³¹⁻³³ Previously^{32,33} we reported atomistic simulations of the location of multiple ions in aqueous nanodroplets with diameter \approx 2 nm - 16 nm at a temperature range of 300 K to 450 K. It was found that in droplets comprising \approx 1000 H₂O molecules, the radial ion distribution (measured from the droplet’s center of mass - COM) is almost uniform. As the droplet size increases, the distribution shows a distinct maximum in the outer droplet layers. The distribution decays almost exponentially toward the droplet’s COM. Toward the droplet exterior, the decay is

determined by the ion size and shape fluctuations.³² The solution of the non-linear Poisson-Boltzmann equation for a spherical geometry³⁴ is used as a reference model to compare with the atomistic simulations. The distributions of multiple ions and biological molecules such as peptides in supercooled droplets are still completely unknown.

The related question of the propensity of ions in a liquid-vapor planar interface has been studied over several decades.³⁵⁻⁴⁹ It is emphasized that the forces that determine the location of multiple ions in a planar interface are not the same as those in charged droplets regardless of their size. The reason is that the conductivity of the aqueous droplets drives the excess ions nearer to the surface and the counterions toward the interior.³³ Another difference arises from the type of fluctuations that a droplet undergoes. Typical fluctuations in a charged droplet, regardless of its size, are conical protrusions on the surface, which are absent in a planar interface.^{50,51} These fluctuations may lead to release of ions from droplets. A single ion in a droplet is always subject to a harmonic potential centered to the droplets’ COM, as we show in this article. Such a force is not present in a planar interface. Detailed chemical interactions (e.g. charge transfer, solvent network) add one more layer of complexity in determining the ion position.

Here we study the radial distribution profiles of a single ion and multiple ions in relation to the solvent organization in supercooled aqueous clusters with sizes that vary from 100 H₂O molecules (corresponding to a diameter of \approx 1.8 nm) to 1100 (diameter \approx 4.0 nm). Our recent computer simulations⁵² for pristine supercooled water clusters have revealed an anomalous, inverted radial density profile emerging for $N \geq 200$ molecules at low temperature, in which a low-density core with relatively good tetrahedral ordering⁵³ is surrounded by a higher density subsurface. These observations have some commonalities with studies of nucleation within droplets and thin films.⁵⁴⁻⁵⁸ We hypothesize that the low density water core in supercooled droplets will differentiate the ion distribution from that at room temperature. This

hypothesis has not been explored earlier.¹⁷

In order to obtain insight into the fundamental forces that determine the location of a single ion, we introduce a reference analytical model of a fluctuating droplet that contains a single ion. To our knowledge, such a reference model is still missing from the literature. In the model the energy of a fluctuating droplet is the sum of the electrostatic energy and surface energy. It predicts that an ion is always subject to a harmonic potential centered at the droplet’s COM. For this reason we name this effect “electrostatic confinement” (EC). The EC effect competes with the geometric confinement. We present the conditions under which the electrostatic confinement is more evident.

Theory of Electrostatic Confinement

Here, we present the key points of an analytical model that provides insight into the forces that determine the location of a single (macro)ion in a droplet. The details of the model are found in Sec. S1 in the SI. In the model we consider a charged dielectric droplet that may undergo shape fluctuations. The charge carrier can be a simple ion such as a Na^+ or a single macroion with bound charge such as a protein or a nucleic acid. The energy of the charged droplet is written as the sum of the electrostatic energy and surface energy.

After some algebra (details are found in Sec. S1 in SI), it is found that the energy (denoted by ΔE_1) related to the distance of the ion from the droplet’s COM is given by

$$\Delta E_1(\|\mathbf{r}\|) = \frac{\varepsilon - 1}{4\pi\epsilon_0\varepsilon(\varepsilon + 2)} \frac{Q^2}{R^3} \|\mathbf{r}\|^2 \quad (1)$$

where Q , R and ε are the charge of the ion, the droplet radius and the relative dielectric constant of the solvent, respectively, ϵ_0 is the vacuum permittivity and $\|\mathbf{r}\|^2 = X_{\text{COM}}^2 + Y_{\text{COM}}^2 + Z_{\text{COM}}^2$ (where $X_{\text{COM}}, Y_{\text{COM}}, Z_{\text{COM}}$ are the coordinates of the droplet’s COM). The energy (1) has the functional form of a harmonic potential.

From this point we would refer to this effect as “electrostatic confinement” (EC). We introduce the spring constant $K(\varepsilon)$ where

$$K(\varepsilon) = \frac{\varepsilon - 1}{4\pi\epsilon_0\varepsilon(\varepsilon + 2)} \frac{Q^2}{R^3}. \quad (2)$$

In Fig. 1 we plot the value of the spring constant as a function of the relative dielectric constant for a droplet comprising 1000 water molecules and an ion. The electrostatic energy has two limiting cases $\varepsilon = 1$ and $\varepsilon = \infty$ when the electrostatic interaction of the ion with the droplet surface vanishes. In the former case the external and internal dielectric constants are equal and the droplet does not perturb the electric field of the ion. In the latter case the electrostatic field is localized in the vicinity of the ion and it is not affected by the droplet surface. As seen in the plot the maximum of the coefficient $K(\varepsilon)$ is attained at $\varepsilon = 1 + \sqrt{3} \approx 2.73$.

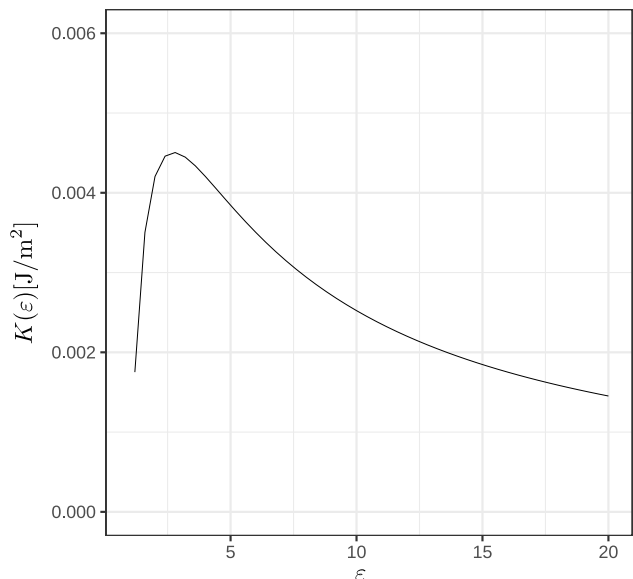


Figure 1: Magnitude of the spring constant (Eq. 2) as a function of the relative dielectric constant ε . The values correspond to an ion of charge $Q = 1e$ in a droplet comprising 1000 water molecules and radius 19\AA . The value of the potential has a maximum at $\varepsilon \approx 1 + \sqrt{3} \approx 2.73$.

If the ion is localized in the droplet interior the Gibbs-Boltzmann distribution of the ion po-

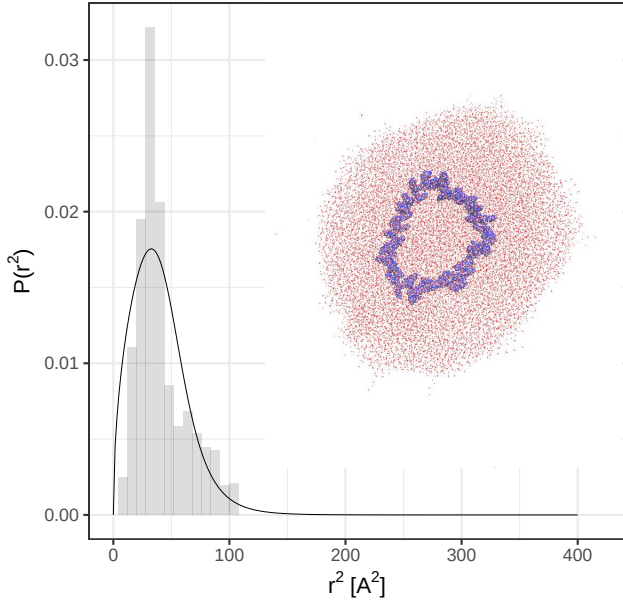


Figure 2: Distribution of the distances of the COM of the cyclic peptide (grey colored histogram) measured from the droplet’s COM. The droplet radius is 3.8 nm and the charge of the peptide is $8e^+$. The solid line is the gamma function fitted to the distribution using the maximum likelihood estimate (MLE). The inset shows a typical snapshot of the droplet composed of 8000 H_2O molecules (red colored) and the cyclic peptide (blue colored).

sitions is given by

$$P(\|\mathbf{r}\|^2) = \frac{2}{\sqrt{\pi}} \left(\frac{K(\varepsilon)}{k_B T} \right)^{3/2} \|\mathbf{r}\| e^{-K(\varepsilon)\|\mathbf{r}\|^2/k_B T}. \quad (3)$$

This probability distribution yields the radial concentration profile of the ion along the droplet radius. The expectation value of the square of the distance of the ion from the center of mass is given by

$$\langle \|\mathbf{r}\|^2 \rangle = \frac{3}{2} \frac{k_B T}{K(\varepsilon)}. \quad (4)$$

The EC is more pronounced when the ion is localized at the center of the droplet, therefore we can write $\langle \|\mathbf{r}\|^2 \rangle / R^2 \ll 1$. Analyzing Eqs. (2) and (4) we conclude that the effect will be more pronounced at low temperature, high charge, small radius and intermediate values of the dielectric constant. Small droplet with high

charge may undergo Rayleigh instability^{59–62} leading to the “star”-shaped droplets⁶³ (see Fig. S2 in SI). If this is an issue in observations we need to increase the droplet radius while keeping constant the value of the Rayleigh parameter $X \sim Q^2/R^3$.⁵¹ To illustrate the EC we model high charges by creating models of charged cyclic peptides. We could have used in the simulations a spherical ion with charge $8e^+$ (or any other charge) instead of a cyclic peptide. The cyclic peptide is preferred because it is an effective way to create a large compact charge, which gives rise to realistic local electric fields that are not high enough to cause water dissociation. In experiments, a single ion with a high charge (e.g. $8e^+$) may give rise to high local electric fields that may lead to water dissociation. The distribution of charge in a cyclic peptide does not cause this problem. DNA and RNA strands are other examples where the effect of the EC will be clearly observed. When a linear nucleic acid is used the droplet size should be large enough so that the linear geometry of the macroion does not affect the droplet’s spherical shape.

Using the maximum value of the K parameter from Fig. 1 we obtain the estimate of the minimal dimensions of the excursions of the ion from its equilibrium position at the center of the droplet $\sqrt{\langle \|\mathbf{r}\|^2 \rangle} \geq 12 \text{ \AA}$. Therefore, for a droplet comprising 1000 water molecules and a single charge $Q = 1e$ the geometric confining effects should be taken into consideration.

In Fig. 2 the distribution of the distance of the center of mass of the peptide relative to the COM of the droplet is plotted. The droplet’s equimolar radius (R_e) is 3.8 nm and the charge is $8e^+$. The distribution tapers off before reaching the droplet surface. Sampling proves to be a challenge in such systems. The simulation time should be much longer than the time for a molecule to diffuse the width of the droplet $Dt_{\text{sim}} \gg R^2$. Typical values of the diffusion coefficient (D) are $\sim 10^{-9} [\frac{\text{m}^2}{\text{s}}]$, hence the simulation time has to be in 10 ns 100 ns range at temperature $T = 300\text{K}$.

In summary, we showed that there is always a force on an ion toward the droplet’s COM. The EC effect is more evident for an ion with

a charge of at least $\pm 3e$ (where e is the elementary positive charge) found in a droplet with a relatively small radius (Fig. S1 in SI). For the EC to become evident the radius size will be equal or moderately larger than the radius at the Rayleigh limit.^{59,61,62} The Rayleigh limit is defined as the point where the electrostatic forces balance the surface forces. For a radius smaller than that at the Rayleigh limit, the droplet shows instability that takes “star”-shapes (Fig. S2 in SI). The star-shapes are minimum energy structures. The EC model can be extended further by including other factors such as the ion size and hydrophobic effects.

Experimental: Models and Simulation Methods

Here we present the main points of the computational methods. A detailed account of the methodology and parameters are found in Sec. S2 in SI. We performed equilibrium molecular dynamics (MD) simulations of aqueous nanodroplets charged with a single ion Na^+ , Li^+ , Cs^+ , F^- , Cl^- , I^- , and multiple Na^+ ions. The droplets range in size from 100 H_2O molecules ($R_e = 0.87$ nm) - 1100 H_2O molecules ($R_e = 2.0$ nm). The temperature of the droplets was set at $T = 200$ K for supercooled droplets and at 300 K (room temperature) except for the 100- H_2O -molecule droplets that were simulated at 260 K instead of 300 K. The MD simulations were performed using GRO-MACS v4.6.1⁶⁴⁻⁶⁷ and NAMD v2.14.⁶⁸ The water molecules are modeled with the TIP4P/2005 (transferable intermolecular potential with four points) model.⁶⁹ We selected the TIP4P/2005 because it reproduces well the density anomaly in liquid water,^{69,70} the liquid-gas surface tension over a broad range of temperatures⁷¹ and the liquid-gas coexistence line in the density-temperature plane.⁷² We also performed a number of simulations with a Drude oscillator-based polarizable model, where the H_2O molecules are represented with the SWM4-NDP model⁷³ and the ions, Na^+ and Li^+ with the CHARMM Drude force field.^{74,75} The equations of motion for the TIP4P/2005 set of simulations

were integrated with a time step of 2.0 fs and for the SWM4-NDP model with 1.0 fs. Each nanodroplet was placed in a closed volume so that it is in equilibrium with its vapor. The volume is large enough to accommodate the droplet’s shape fluctuations. The simulations were carried out in the canonical ensemble – constant number of molecules (N), volume, and T . The trajectories were visualized using VMD 1.9.4a47.⁷⁶

To analyze the features of the radial distribution (concentration) profiles of the ions in relation to the water structure, we use several parameters: (a) the density of water as determined from the Voronoi volumes associated with each water molecule, denoted by $\rho_V(r)$ (where r denotes the distance from the droplet’s COM); (b) the tetrahedral order parameter, denoted by $q_T(r)$, and (c) the distance to the fifth nearest neighbor O of a given O atom denoted by d_5 .

The parameter $q_T(r)$ is defined as follows. Initially, the tetrahedral order parameter,⁷⁷ at the level of a single particle is defined as,

$$q_i = 1 - \frac{3}{8} \sum_{j=1}^3 \sum_{k=j+1}^4 \left[\cos \psi_{jik} + \frac{1}{3} \right]^2, \quad (5)$$

where ψ_{jik} is the angle between an oxygen atom i and its nearest neighbor oxygen atoms j and k within a distance of $r_{cut} = 0.35$ nm. The radial function $q_T(r)$ as the average value of q_i for all molecules within a spherical shell enclosed within $r \pm \Delta r/2$, where $\Delta r = 0.05$ nm. Similarly, we report results for $d_5(r)$, the average distance to the fifth O neighbor for O atoms located in the same spherical shell centered at r . We note that we find sometimes slight, but no significant differences for $\rho(r)$, $\rho_v(r)$, $q_T(r)$ and $d_5(r)$ whether an ion is present or not, and therefore use well-sampled data for these quantities for pure water taken from previous studies.^{52,53}

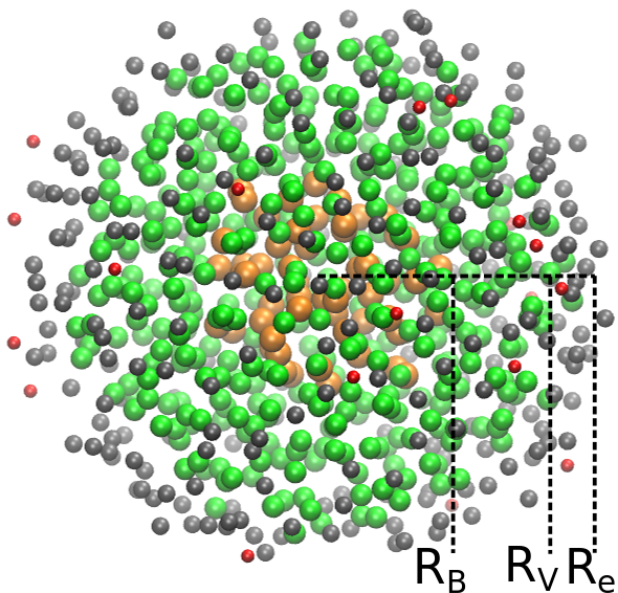


Figure 3: Regions in a typical snapshot showing O atomic sites of a system composed of 776 H_2O molecules- Na^+ at 200 K. From the center of mass to a distance $r = R_B$, the core structure (orange-colored) is characterized by a bulk-like, low-density tetrahedral network. The subsurface region $R_B < r < R_V$ (green-colored), is characterized by a higher density, lower tetrahedrality, and structure that changes with r . Surface atoms (grey-colored) in $R_V < r < R_e$ have a large Voronoi volume. The remaining atoms (red-colored) are found in $r > R_e$, where R_e is the equimolar radius. The determination of R_B and R_V is illustrated in Fig. 4 and discussed in the text. The lower-density core and higher-density subsurface is a structural feature emerging at low T and $N \geq 200$.

Results

Single ion

The main idea of the present article is that the low-density tetrahedral network that forms at sufficiently low T in the core of sufficiently large nanodroplets tends to expel certain ions to the relatively higher-density and more disordered subsurface. Fig. 3 illustrates this structure for the case of an $N = 776$ nanodroplet. The density structure of the nanodroplet is approximately the same for the nanodroplet whether

it contains a single, several or no ions. Using a $N = 776\text{-Na}^+$ nanodroplet as an example, it is found that at 200 K, the $0 < r < R_B = 7.4 \text{ \AA}$ region includes on average 57.14 oxygen sites yielding a number density $33.66 \pm 0.15 \text{ nm}^{-3}$. The subsurface, $R_B < r < R_V = 14.8 \text{ \AA}$ includes on average 410.62 O sites yielding a number density $34.56 \pm 0.15 \text{ nm}^{-3}$. At 300 K, the density in the core is $34.38 \pm 0.15 \text{ nm}^{-3}$ and in the subsurface $34.14 \pm 0.15 \text{ nm}^{-3}$, and thus the difference at 200 K is inverted and significantly larger than at 300 K.

A more quantitative description is provided in Fig. 4, which shows the relation of the water structure and the probability density of the ion at 300 K (red curves) and 200 K (black curves). Fig. 4 (a) shows the H_2O radial density ($\rho(r)$) using the physical volume. Even though $\rho(r)$ profiles are typically used to identify a cluster's boundary, they may mask certain features. The decrease in the density profile close to the cluster's boundary masks the role of the shape fluctuations. Also, the fact that the profiles are built around the cluster's COM, which is not one of the molecular entities in the system, may overemphasize the layered structure of the solvent at supercooling. In larger particles (e.g. aerosols) the plot will provide the average density of the droplet as a function of radius and layering will not be present. For this reason, we use additional measures of the solvent structure such as the Voronoi volume (Fig. 4 (a) and (b)), q_T (Fig. 4 (c)) and d_5 (Fig. 4 (d)). Note that for $r < 0.2 \text{ nm}$, good statistics are difficult to obtain for all radial quantities, and results in this regime are quite noisy. The density using the Voronoi volume ($\rho_V(r)$) is also shown in Fig. 4 (a). The main feature of $\rho_V(r)$ is that it decays rapidly for surface atoms – those with large Voronoi volumes that extend outside the nanodroplet. To define a surface region we find R_V such that $\rho_V(R_V) = \rho(R_e)$. Given this, approximately two thirds of the molecules at $r = R_V$ have unbounded Voronoi volumes. In Fig. 4 (b) we show a close-up of $\rho_V(r)$. While monotonically decreasing with r at large T , at low T , $\rho_V(r)$ is approximately constant for $r < R_B$ and then increases to a maximum at $r = R_P$. We choose $r = R_P$ as a representa-

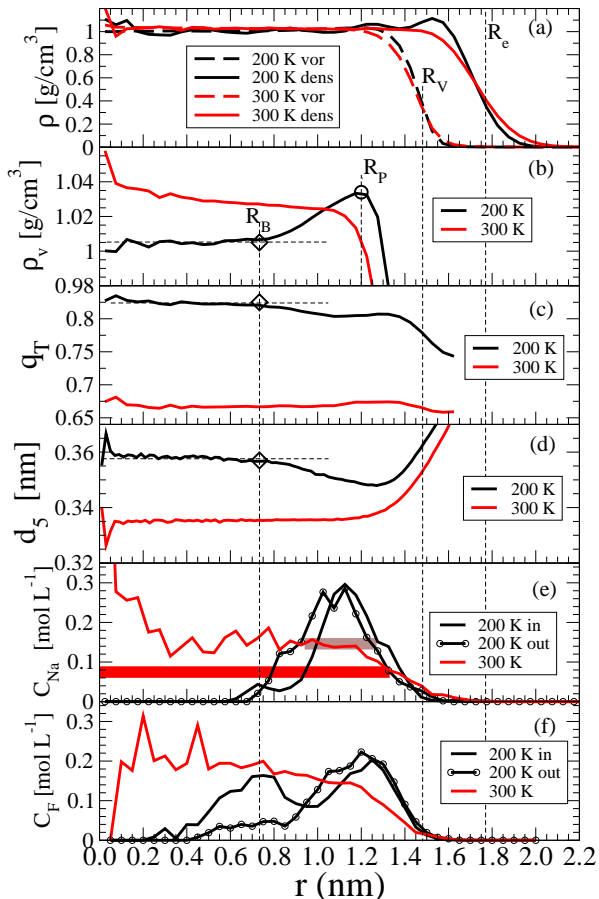


Figure 4: Structure of pristine water droplet, single Na^+ and single F^- distributions for $N = 776$ at $T = 200$ K (black line) and $T = 300$ K (red line). Shown as functions of r are (a) density ρ and density determined from Voronoi volumes ρ_V ; (b) a close up of ρ_V ; (c) tetrahedral order parameter q_T ; (d) distance of the fifth O neighbor d_5 ; (e) Na^+ concentration, C_{Na} , for a single ion, which for 200 K includes results from starting the ion at the centre (in) and at the surface (out); and (f) same as (e) but for F^- . In panel (b), R_P marks the maximum in ρ_V , a feature representative of the subsurface at low T . The horizontal bars in panel (e) approximate the spatial extent of C_{Na} for 200 K (brown) and 300 K (red), and appear in Fig. 5. See details in the text.

tive feature of the subsurface, which now by default occupies $R_B < r < R_V$. Fig. 4 (c) and Fig. 4 (d), showing $q_T(r)$ and $d_5(r)$, respectively, likewise show a bulk-like core with uniform properties for $r < R_B$ and a more dis-

ordered subsurface. The parameter d_5 , a more indirect measure of the quality of the tetrahedral network, shows a more disordered structure in the vicinity of the subsurface density peak at low T . We note that $q_T(r)$ begins to increase beyond a minimum located at 1.6 nm, a location clearly in the surface layer where d_5 is quite high and ρ_V is nearly zero. We thus cut off the $q_T(r)$ at this minimum, as the increase is not indicative of increased tetrahedral order.

Fig. 4 (e) shows Na^+ concentration $C_{\text{Na}}(r)$ at 200 K and 300 K when a single Na^+ ion is present in the nanodroplet. At low T , $C_{\text{Na}}(r)$ as obtained from starting the ion near the centre and starting near the surface are compared – thus showing the degree of equilibration we achieve. At $T = 300$ K, $C_{\text{Na}}(r)$ is approximately constant in the interior of the droplet, and begins to decay within the subsurface, becoming small by R_V and decaying to zero significantly before $\rho(r)$ does. At room temperature the Na^+ concentration profile is consistent with the EC model. Because of the low charge, the geometric confinement effect dominates over the force toward the droplet’s COM. For this reason, the Na^+ radial distribution does not distinctly peak at the droplet’s COM, but it appears to be almost uniform with a slight increase toward the droplet’s COM.

Fig. 4 (e) shows a significant difference in $C_{\text{Na}}(r)$ at 200 K. Rather than being almost uniform, $C_{\text{Na}}(r)$ has a peak located within 0.2 nm from R_P . Thus, we see that in a nanodroplet with a heterogeneous radial density, as determined by $\rho_V(r)$, the single Na^+ ion tends to reside in the highest density environment for most of the time. This tendency is consistent with the fact that for constant T and polarization factor (degree of dipole ordering),⁷⁸ the dielectric constant increases with increasing density.

The thick horizontal bars shown in Fig. 4(e) measure the approximate extents of $C_{\text{Na}}(r)$ for low (brown) and high (red) T , and are drawn between C_{Na} values of half the peak or plateau height. For 300 K, notwithstanding noise below $r = 0.2$ nm, the distribution extends to the center of the droplet, and so the left end point of the red bar is at $r = 0$. These horizontal bars are replotted vertically in Fig. 5 along

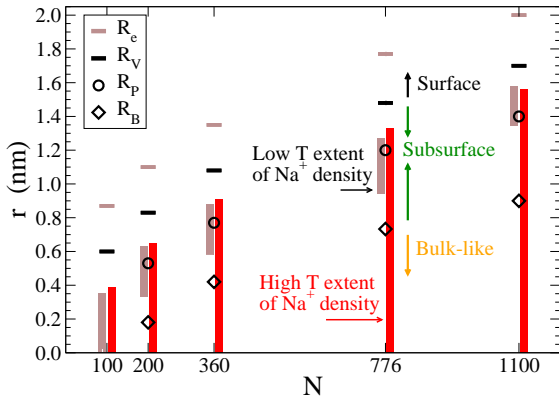


Figure 5: Radial features of nanodroplets comprising N water molecules and a single Na^+ . The features shown for each N are determined as illustrated in Fig. 4 for $N = 776$.

with R_B , R_P , R_V and R_e , for other nanodroplet sizes. The detailed Na^+ radial distribution profiles and the histograms of the raw data for the various droplet sizes are shown in Figs. S3 and S4, respectively, in SI. Fig. 5 shows the same trend in the structure of the H_2O and the location of the ions as found for $N = 776$. Measures of structure for low temperature ($T = 200$ K) as those shown in Fig. 4 and in detail in Fig. S4 in SI are summarized in Fig. 5. The convergence of the trajectories for Na^+ starting on the surface and the droplet’s COM is shown in Fig. S5 in SI. The surface thickness is estimated to be $R_e - R_V \approx 0.3$ nm and the subsurface thickness $R_V - R_B \approx 0.7 - 0.8$ nm for all sizes studied. It is noted that the cluster of $N = 100$ does not show a tetrahedrally organized core.

Similarly to Na^+ , at 300 K, F^- (Fig. 4 (f)) and Li^+ (Fig. S6 in SI) show higher concentration in $0 < r < R_B$. Behavior consistent with our present study for F^- at 300 K has been reported in Ref. ^{15,42} for clusters composed of 124-145 H_2O molecules. However, these systems are too small to show the effect of a core and subsurface in the ion location. We find that at 200 K, the maximum of the F^- concentration is shifted into the subsurface ($R_B < r < R_V$), and similarly for Li^+ .

In Fig. 6, we summarize how the concentration changes in the bulk core ($0 < r < R_B$),

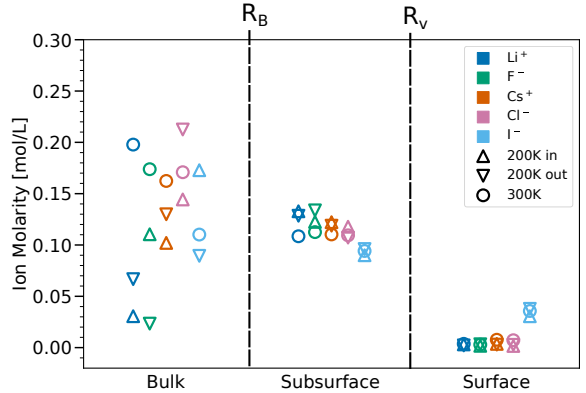


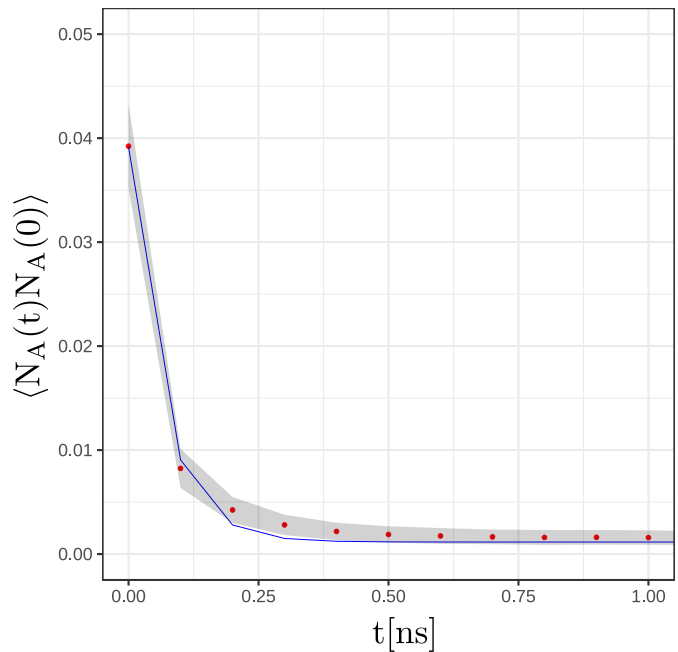
Figure 6: Ion concentrations in the core, subsurface and surface regions of an $N = 776$ nanodroplet at 300 K (circles) and 200 K (triangles pointing up for simulations where the ion begins at the COM, downward for starting at the surface).

subsurface ($R_B < r < R_V$) and surface ($R_V < r < R_e$) regions on changing T from 300 K to 200 K for ions other than Na^+ in an $N = 776$ nanodroplet. The details of the concentration profiles as a function of the distance from the droplet’s COM and the histograms of the raw data are shown in Figs. S6 and S7, respectively, in SI. Fig. 6 shows a significant decrease in the core concentration, and commensurate increase in the subsurface concentration, for Li^+ and F^- , and, to a lesser extent, for Cs^+ as well. The larger anions Cl^- and I^- show no significant change.

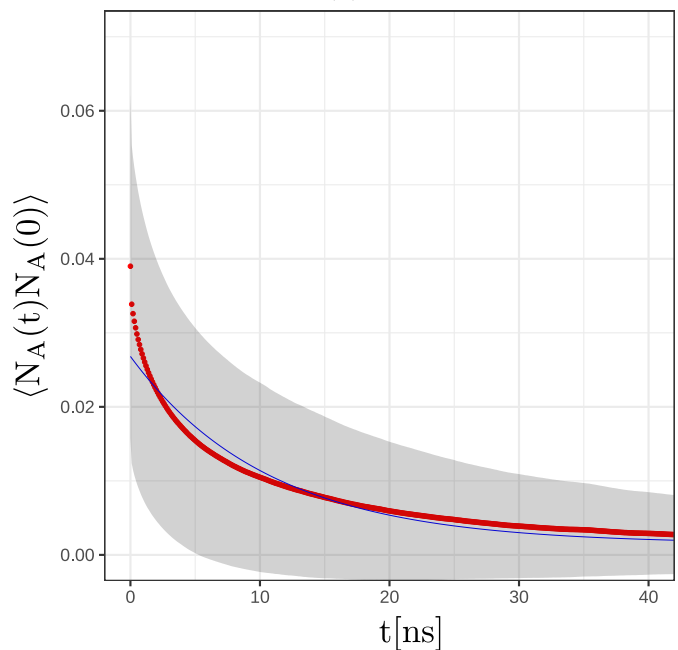
In order to understand better the concentration changes at 200 K we discuss the direct monitoring of the transition events between the core and subsurface at 200 K, which are shown in Figs. S8, S9, and 10 in SI. Li^+ and F^- show only 1-2 events entering the core over a $2 \mu\text{s}$ (considering two MD trajectories of $1 \mu\text{s}$ each) production run, Cs^+ shows 3-4 events and Cl^- , I^- 5-6 events. During these rare events all the ions that we study are trapped within the core for at least 20 ns. Thus, differently from 300 K, where the large probability density in the core appears due to the frequent transitions between core and subsurface (Fig. S11 in SI), at 200 K, an increase in the probability density in the core appears due to the long residence time in this region.

The time evolution of the Cl^- transition events (Figs. S9 (a) in SI) does not show specific preference for the interior or the surface at both temperatures. A similar propensity for Cl^- ions was pointed out by Zhao et al.¹⁵ who performed simulations of halogen anions in a cluster of 124 H_2O molecules at room temperature and at supercooling using Born-Oppenheimer (BO) MD simulations. In BO-MD the interactions are described by quantum density functional theory (DFT). The agreement between the results supports the validity of TIP4P/2005 to predict the location of the ions. The direct monitoring of the transitions, Fig. S9 in SI, shows that Cl^- and I^- interact more than the other ions with the boundary of the bulk core ($4.0 \text{ \AA} < r < 7.4 \text{ \AA}$) when they are in the subsurface, which may be the reason that allows them to make more frequent transition into the core than other ions. The Cs^+ ion, even though a chaotropic ion like Cl^- and I^- , shows some features similar to Li^+ , in that it does not frequently access the boundary of the bulk-like core as Cl^- and I^- do. In the rare transitions to the core, Cs^+ remains trapped for a significant amount of time and for this reason its concentration profile appears bi-modal. A general observation from all the trajectories is that the crossing of the core is relatively faster than the residence time within the core, which indicates the presence of high potential energy barriers. The transition paths can be step-wise or rapid, which reflect the variety of pathways that can be followed by the ions in and out of the core region.

Now we examine the time correlation function for the exchange of the H_2O molecules surrounding F^- in $N = 776$. Following the approach of D. Chandler in Ref.⁷⁹ we define a state variable, N_A which is 1 if a H_2O molecule is within a sphere of radius 6.0 \AA with center the F^- ion and zero otherwise. Using this state variable we compute the correlation function $\langle N_A(t)N_A(0) \rangle$. The correlation functions at 300 K and 200 K are shown in Fig. 7. The correlation functions decay to the ratio of the number of H_2O molecules contained in the volume of radius 6.0 \AA over the total number of molecules in the droplet. We find that the de-



(a)



(b)

Figure 7: Time correlation function (red line) of H_2O molecules coordinating F^- in $N = 776$ cluster at (a) $T = 300 \text{ K}$ and (b) $T = 200 \text{ K}$. The grey region is one standard deviation. The blue line is the exponential fitting to the simulation data given by (a) $y = 1.76 \times 10^{-3} + 0.038 \exp(-t/0.0637)$, (b) $y = 1.49 \times 10^{-3} + 0.0253 \exp(-t/10.7)$.

cay time at 300 K is 64 ps and at 200 K 10.7 ns. The ratio of the decay time at 200 K to 300 K is

≈ 200 times larger than the ratio of the average velocities of the molecules at the two temperatures. The long residence time of the ions in the core and subsurface region is consistent with the decay time of the correlation function. Thus, in addition to structural and energetic factors that determine ion location, the two-orders-of-magnitude slowing down in dynamics at low T may be necessary to consider when time scales relevant to an experiment become comparable to the decay time. Further complexities arise from the fact that dynamics at the surface and subsurface should be significantly faster than in the core. We have not addressed the radial dependence of the dynamics here, but we expect to address this in the future.

To test the effect of the force field in the different density regions, simulations were performed with a Drude oscillator-based force field,⁷³ which uses the SWM4-NDP H₂O model. The ion distribution profiles for a single Na⁺ and Li⁺ in an N=880 H₂O droplet at 350 K and 200 K are presented in Fig. S14 and Fig. S15 in SI. At high temperature, similar to the runs with TIP4P/2005, the Na⁺ and Li⁺ radial distributions are uniform in the core and in part of the subsurface. The Li⁺ shows a preference toward the center. In both the TIP4P/2005 and SWM4-NDP the concentration of the ions starts to increase at 1.6 nm, which indicates that the depth from the surface is in good agreement between the two models. At low temperature it has been found that POL3 and SWM4-NDP are not suitable for ice-liquid simulation - they lead to a poor representation of ice.^{80,81} We note here that the temperature in different molecular models may not correspond to the same physical state of the cluster. At 200 K, simulations of bulk solution have shown that SWM4-NDP is close to the point of maximum density of water.^{80,81} We have confirmed that even in clusters at 200 K the density is at its maximum. At 350 K, the density in the core is $32.79 \pm 0.15 \text{ nm}^{-3}$ and in the subsurface $32.39 \pm 0.15 \text{ nm}^{-3}$ while at 200 K, the density is $36.15 \pm 0.15 \text{ nm}^{-3}$ and $35.85 \pm 0.15 \text{ nm}^{-3}$, respectively. Interestingly, both the Li⁺ and Na⁺ distributions using the polarizable model show their maximum in the subsurface, simi-

larly to the TIP4P/2005. Disregarding the unrealistic nature of the density in the cluster for SWM4-NDP, this example demonstrates that there may be an optimal density for solvation of the ions.

Regarding the relation of the subsurface structure in a droplet to that of a planar surface we note that densification at supercooling also occurs for a planar interface.^{57,82} In the temperature range of our study, the clusters are still in the liquid state. The experiments of Pradzynski et al. have shown the possibility of ice formation in clusters composed of several hundreds of water molecules.⁷ The authors estimated that the temperature of the clusters is 90 K-115 K. We expect that in order to see a phase transition in the systems that we study, we should decrease the temperature below 200 K. In the analysis of surface layers it will be challenging to distinguish small-particle surface melting from size-dependent melting.⁸³

The expulsion of the ions from the core is reminiscent of brine rejection from ice, where upon crystallization ions are expelled into the liquid.^{84,85} While liquid water lacks the long-range order of the crystal, the low-density form of the liquid, like ice, possesses a network structure, characterized by a first sharp diffraction peak in the structure factor arising from a high degree of tetrahedrality.⁸⁶⁻⁸⁸ The value of q_T of deeply supercooled liquid water is comparable to that of ice.^{53,84} For nanodroplets, the more disordered and denser subsurface appears to play the role of liquid water in usual brine rejection at freezing. We expect that the dynamics and the precise steps of the ion rejection mechanisms from the low-density core in nanodroplets will be different from those in bulk ice. It is noted that in simulations of brine rejection,⁸⁴ Na⁺ is rejected faster than Cl⁻, with Cl⁻ being more than twice as likely to be incorporated into the crystal lattice, an observation not dissimilar to what we see in terms of Cl⁻ remaining in the low-density liquid nanodroplet core, although sampling equilibrium distributions in the case of brine rejection is certainly more difficult.

Multiple Na⁺ ions

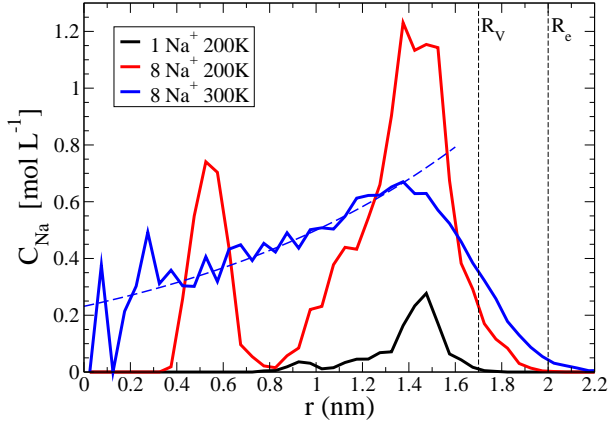


Figure 8: C_{Na} profile along the droplet radius (measured from the COM) of a single ion (at 200 K) and 8 Na⁺ ions (at 200 K and 300 K) in a droplet comprised 1100 H₂O molecules. Dashed blue line is the prediction of Eq. 6 for the droplet at 300 K (details in the text).

Figure 8 shows the radial distributions of multiple ions at $T = 300$ K and 200 K in droplets comprising 1100 H₂O molecules. The same plot for a system of 776 H₂O molecules - 5 Na⁺ ions is shown in Fig. S16 in SI. At $T = 300$ K the distributions (for 1100 and 776 H₂O molecules) are almost uniform with an incipient broad maximum appearing in the outer layers of the droplet.

Solution of the Non-linear Poisson-Boltzmann (NPB) equation³⁴ for a rigid spherical geometry suggests that toward the droplet interior the ion distribution will show an exponential decay

$$n(r) = n(R) \exp[(r - R)/\lambda_{\text{PB}}] \quad (6)$$

where n is the ion number density, R is the sphere radius (here taken to be equal to R_e) and r is the distance from the droplet center. λ_{PB} is given by

$$\lambda_{\text{PB}} \approx \frac{\epsilon k_B T}{\sigma q} \quad (7)$$

where k_B is Boltzmann constant, T is temperature, ϵ is the permittivity of the medium, $q = me$ is the charge of an ion and σ is the sur-

face charge density given by $\sigma = \frac{|Z|e}{4\pi R^2}$ ($|Z|e$ is the total droplet charge). In finding the surface charge density we assume that all the charge is in the surface. The larger the λ_{PB} the slower the ion distribution decay. One of the reasons that the simulated ion decay may deviate from the theoretical prediction is the droplet's shape fluctuations. For this reason, we expect that the exponential decay will manifest more clearly in larger droplets at lower temperature. We note that in the larger droplets the effect of the counterions in λ_{PB} has also to be considered.³⁴ Evidently, the higher temperature will lead to a slower ion decay. For 1100 H₂O - 8 Na⁺ ions at $T = 300$ K the distribution decays (toward the droplet's COM) as an exponential function fitted by $0.40 \exp(-(1.37-r)/1.3)$, where $\lambda_{\text{PB}} \approx 1.3$ nm (note: to convert from $n(r)$ in nm⁻³ to $C_{\text{Na}}(r)$ in mol/L, one should multiply $n(r)$ by $10/6.022$). Equation 7 with dielectric constant of water equal to 75, yields $\lambda_{\text{PB}} \approx 0.8$. In droplets of up to a few thousands of water molecules the effect of shape fluctuations is significant, therefore, we interpret the value of λ_{PB} only in a qualitative manner. A value of λ_{PB} in the range of 0.8 nm (theoretical estimate)-1.3 nm (from fitting) is comparable in magnitude with the droplet radius ($R_e = 2.0$ nm), which indicates that the radial distribution function will decay slowly toward the COM. The predicted slow decay is indeed found in the simulations. The ion distribution at $T = 200$ K decays in a way that cannot be analyzed using the NPB predictions at the lower temperature. The multiple ions similarly to the single ion are expelled from the drop's core and their distribution shows a maximum at the same location as the single ion (Fig. 8). The distribution shows two peaks at a distance 0.52 nm and at 1.5 nm. The lower intensity peak at 0.52 nm corresponds to a single ion that exchanges location with the outer ions (found at ≈ 1.5 nm). The mobility of the inner ion indicates that the appearance of the two peaks is not due to a metastable state.

Conclusions

We found that in supercooled aqueous droplets, a heterogeneous solvent structure leads to a different ion radial distribution relative to that at a room temperature. Specifically, we demonstrated that the interior tetrahedral network that forms at supercooling expels cosmotropic ions (Na^+ , Li^+ , F^-) from the core region to the more disordered subsurface. The radial distribution of chaotropic ions (Cl^- , I^- , Cs^+) appear to be affected less by the presence of the bulk-structured core. They also spend most of the time in the subsurface from where they make rare incursions to the core region. Once inside the core, they reside there for a significant amount of time.

The atomistically simulated ion radial distributions are supported by a reference analytical model that predicts the location of an ion in a fluctuating droplet. The theory finds that an ion (regardless of its nature) is always subject to a harmonic potential centered at the droplet's center of mass. This electrostatic confinement effect is more evident in certain droplet dimension and ion charge. In the supercooled nanodroplets the model predictions deviate from the simulated ion distributions due to the specific organization of the solvent that is currently not included in the analytic model.

We expect the effect of the heterogeneity in the solvent structure to appear even in the larger droplet sizes. In microdroplets, where thermodynamics of the phase transitions will be similar to that in the bulk solution, ice may form in the interior and then the ions will be expelled most likely in a similar manner to the brine rejection from bulk ice. In a planar surface, where liquid layers cover ice, the dependence of the thickness and ordering of the liquid surface layer on temperature has been studied for several decades.^{89,90} A similar investigation for the subsurface and surface layers is still missing for the nanodroplets.

The present study opens up the discussion on several questions. Evaporative cooling of droplets is a process that has been reported to be important in a droplet's lifetime in ionization methods used in native mass spectrometry.

The implications of the distribution of multiple ions in the subsurface in a Rayleigh fission and ion-evaporation mechanism have to be examined. We have found that a conical deformation is a key structure in the mechanism of ion emission.⁵¹ An intriguing question is whether the formation of a conical deformation in the droplet that emits ions is affected by the low density liquid at supercooling or an ice interior. A related question is whether the Rayleigh limit of a supercooled droplet changes since the conducting region for certain ions is restricted to the subsurface and surface instead of exploring the volume of the entire droplet. In a long time, the droplet is expected to be a conductor, since the ion still make rare visits to the core. In an intermediate length of time, which may be critical for charging of macromolecules of instance, the properties of the droplet may deviate from those of a good conductor. A study on these questions will be relevant to atmospheric chemistry, native mass spectrometry and the physics of jets.

We anticipate our study to provide the starting point for investigating the structure of the supercooled droplets containing unstructured peptides and complexes of ions. Several possible scenarios are envisioned that may affect the charge states of macromolecules. On the one hand, if a macromolecule and simple ions are expelled to the subsurface, the macromolecule will be exposed to a higher concentration of ions and different structure of solvent than that at room or elevated temperature. Thus, their charge state and release mechanism will be determined by the distinct chemical features of the subsurface. Because of the higher concentration of ions in the subsurface than at room or elevated temperature, for certain macromolecules, a "salting-out" release pathway may open up that expels them to the vapor phase. Clusters containing solvated NaCl or $[\text{Na}_2\text{Cl}]^+$ complexes where the ions are in their contact-ion pair form may be also expelled. This is a new idea that has not been explored before as a possible mechanism of release of macroions from droplets. If macroions are released via a salting-out path, or if the counterions are released in the form of complexes

with the co-ions they will not form adducts with the macromolecules. This outcome is in agreement with still unresolved observations in native mass spectrometry experiments. On the other hand, if a macromolecule (regardless of its shape) is trapped in a glassy core its diffusion toward the surface will be delayed and its exposure to ions will be altered, which will in turn affect its charge state. In this case, a charged-residue mechanism is more likely to be followed in the charging of the macromolecule. We currently explore these new possible macroion release mechanisms. We envisage that studies in this direction will assist in interpreting ion mobility-mass spectrometry data on the detection of the conformations of macromolecules originating from the bulk solution and will provide insight into the chemistry of atmospheric aerosols.

Supporting Information

(S1) Derivation of the electrostatic confinement (EC) model and comparison with atomistic simulations of an ion in a droplet. (S2) Details of the computational methods and models. (S3) Water density and structure, and single Na^+ radial concentration for various droplet sizes (S4) Evidence of the convergence of the simulation data, and radial probability density (concentration) profiles for I^- , Cl^- , F^- , Li^+ , Cs^+ in room temperature and supercooled nanodroplets. (S5) Radial distribution functions for ion-Oxygen of H_2O and ion-Hydrogen of H_2O . (S6) Radial probability density (concentration) profiles of ions in supercooled and room temperature nanodroplets using a polarizable molecular model. (S7) Multiple-ion radial concentration profiles in supercooled and room temperature nanodroplets.

Acknowledgments

S.C. thanks Prof. D. Frenkel, Department of Chemistry, University of Cambridge, UK, and Dr. Anatoly Malevanets, The University of Western Ontario for discussions on the stability of charged systems. Professor D. Russell,

Department of Chemistry, Texas A & M University is thanked for pointing out the variable temperature ESI source and the role of cold droplets in transferring the protein conformations for MS analysis. V.K. acknowledges the province of Ontario and the University of Western Ontario for the Queen Elizabeth II Graduate Scholarship in Science and Technology. I.S.-V. thanks the Departments of Applied Mathematics and Chemistry at Western University for sabbatical hosting. We acknowledge the financial support from Natural Sciences and Engineering Research Council (Canada). Computational resources were provided by ACENET and Compute Canada.

References

- (1) Raab, S. A.; El-Baba, T. J.; Woodall, D. W.; Liu, W.; Liu, Y.; Baird, Z.; Hales, D. A.; Laganowsky, A.; Russell, D. H.; Clemmer, D. E. Evidence for Many Unique Solution Structures for Chymotrypsin Inhibitor 2: A Thermodynamic Perspective Derived from vT-ESI-IMS-MS Measurements. *J. Am. Chem. Soc.* **2020**, *142*, 17372–17383.
- (2) Bain, R. M.; Pulliam, C. J.; Cooks, R. G. Accelerated Hantzsch electrospray synthesis with temporal control of reaction intermediates. *Chem. Sci.* **2015**, *6*, 397–401.
- (3) Ingram, A. J.; Boeser, C. L.; Zare, R. N. Going beyond electrospray: mass spectrometric studies of chemical reactions in and on liquids. *Chem. Sci.* **2016**, *7*, 39–55.
- (4) Sahraeian, T.; Kulyk, D. S.; Badu-Tawiah, A. K. Droplet Imbibition Enables Non-Equilibrium Interfacial Reactions in Charged Microdroplets. *Langmuir* **2019**, *35*, 14451–14457.
- (5) Lee, S.-W.; Freivogel, P.; Schindler, T.; Beauchamp, J. Freeze-dried biomolecules: FT-ICR studies of the specific solvation of functional groups and clathrate formation observed by the slow evaporation of water from hydrated peptides and model compounds in the gas phase. *J. Am. Chem. Soc.* **1998**, *120*, 11758–11765.
- (6) Schindler, T.; Berg, C.; Niedner-Schatteburg, G.; Bondybey, V. E. Heterogeneously catalyzed hydrolysis of chlorine nitrate: Fourier-transform ion cyclotron resonance investigations of stratospheric chemistry. *J. Chem. Phys.* **1996**, *104*, 3998–4004.
- (7) Pradzynski, C. C.; Forck, R. M.; Zeuch, T.; Slavíček, P.; Buck, U. A fully size-resolved perspective on the crystallization of water clusters. *Science* **2012**, *337*, 1529–1532.
- (8) Stachl, C. N.; Williams, E. R. Effects of temperature on Cs⁺ (H₂O)₂₀ clathrate structure. *J. Phys. Chem. Lett.* **2020**, *11*, 6127–6132.
- (9) Cooper, R. J.; DiTucci, M. J.; Chang, T. M.; Williams, E. R. Delayed onset of crystallinity in ion-containing aqueous nanodrops. *J. Am. Chem. Soc.* **2016**, *138*, 96–99.
- (10) Lu, D.; Singer, S. J. Ion solvation in model polar clusters. *J. Chem. Phys.* **1996**, *105*, 3700–3714.
- (11) Gorlova, O.; DePalma, J. W.; Wolke, C. T.; Brathwaite, A.; Odbadrakh, T. T.; Jordan, K. D.; McCoy, A. B.; Johnson, M. A. Characterization of the primary hydration shell of the hydroxide ion with H₂ tagging vibrational spectroscopy of the OH⁻-(H₂O)_{n=2,3} and OD⁻-(D₂O)_{n=2,3} clusters. *J. Chem. Phys.* **2016**, *145*, 134304.
- (12) Hecce, D. H.; Perera, L.; Darden, T. A.; Sagui, C. Surface solvation for an ion in a water cluster. *J. Chem. Phys.* **2005**, *122*, 024513.
- (13) Perera, L.; Berkowitz, M. L. Ion solvation in water clusters. *Z. Phys. D Atom Mol. Cl.* **1993**, *26*, 166–168.
- (14) Thauay, F.; Ohanessian, G.; Clavaguera, C. Dynamics of ions in a water drop using the AMOEBA polarizable force field. *Chem. Phys. Lett.* **2017**, *671*, 131–137.
- (15) Zhao, Y.; Li, H.; Zeng, X. C. First-principles molecular dynamics simulation of atmospherically relevant anion solvation in supercooled water droplet. *J. Am. Chem. Soc.* **2013**, *135*, 15549–15558.
- (16) Hagberg, D.; Brdarski, S.; Karlström, G. On the solvation of ions in small water droplets. *J. Phys. Chem. B* **2005**, *109*, 4111–4117.

- (17) Burnham, C. J.; Petersen, M. K.; Day, T. J.; Iyengar, S. S.; Voth, G. A. The properties of ion-water clusters. II. Solvation structures of Na⁺, Cl⁻, and H⁺ clusters as a function of temperature. *J. Chem. Phys.* **2006**, *124*, 024327.
- (18) Makov, G.; Nitzan, A. Solvation and ionization near a dielectric surface. *J. Phys. Chem.* **1994**, *98*, 3459–3466.
- (19) Fifen, J. J.; Agmon, N. Structure and spectroscopy of hydrated sodium ions at different temperatures and the cluster stability rules. *J. Chem. Theory Comput.* **2016**, *12*, 1656–1673.
- (20) Galib, M.; Baer, M.; Skinner, L.; Mundy, C.; Huthwelker, T.; Schenter, G.; Benmore, C.; Govind, N.; Fulton, J. L. Revisiting the hydration structure of aqueous Na⁺. *J. Chem. Phys.* **2017**, *146*, 084504.
- (21) Perera, L.; Berkowitz, M. L. Structure and dynamics of Cl-(H₂O)₂₀ clusters: The effect of the polarizability and the charge of the ion. *J. Chem. Phys.* **1992**, *96*, 8288–8294.
- (22) Perera, L.; Berkowitz, M. L. Erratum: Many-body effects in molecular dynamics simulations of Na⁺ (H₂O)_n and Cl⁻ (H₂O)_n clusters [J. Chem. Phys. 95, 1954 (1991)]. *J. Chem. Phys.* **1993**, *99*, 4236–4237.
- (23) Perera, L.; Berkowitz, M. L. Many-body effects in molecular dynamics simulations of Na⁺ (H₂O)_n and Cl⁻ (H₂O)_n clusters. *J. Chem. Phys.* **1991**, *95*, 1954–1963.
- (24) Caleman, C.; Hub, J. S.; van Maaren, P. J.; van der Spoel, D. Atomistic simulation of ion solvation in water explains surface preference of halides. *Proc. Natl. Acad. Sci. U.S.A.* **2011**, *108*, 6838–6842.
- (25) Werhahn, J. C.; Akase, D.; Xantheas, S. S. Universal scaling of potential energy functions describing intermolecular interactions. II. The halide-water and alkali metal-water interactions. *J. Chem. Phys.* **2014**, *141*, 064118.
- (26) Vaitheeswaran, S.; Thirumalai, D. Hydrophobic and ionic interactions in nano-sized water droplets. *J. Am. Chem. Soc.* **2006**, *128*, 13490–13496.
- (27) Harder, E.; Roux, B. On the origin of the electrostatic potential difference at a liquid-vacuum interface. *J. Chem. Phys.* **2008**, *129*, 12B613.
- (28) Fracchia, F.; Del Frate, G.; Mancini, G.; Rocchia, W.; Barone, V. Force field parametrization of metal ions from statistical learning techniques. *J. Chem. Theory Comput.* **2018**, *14*, 255–273.
- (29) Kwan, V.; Consta, S. Molecular Characterization of the Surface Excess Charge Layer in Droplets. *J. Am. Soc. Mass Spectrom.* **2021**, *32*, 33–45, PMID: 32597645.
- (30) Duignan, T. T.; Mundy, C. J.; Schenter, G. K.; Zhao, X. S. Method for Accurately Predicting Solvation Structure. *J. Chem. Theory Comput.* **2020**, *16*, 5401–5409.
- (31) Zdrali, E.; Okur, H.; Roke, S. Specific ion effects at the interface of nanometer-sized droplets in water: structure and stability. *J. Phys. Chem. C* **2019**, *123*, 16621–16630.
- (32) Kwan, V.; Malevanets, A.; Consta, S. Where do the ions reside in a highly charged droplet? *J. Phys. Chem. A* **2019**, *123*, 9298–9310.
- (33) Kwan, V.; Consta, S. Bridging electrostatic properties between nanoscopic and microscopic highly charged droplets. *Chem. Phys. Lett.* **2020**, 137238.
- (34) Malevanets, A.; Consta, S. Variation of droplet acidity during evaporation. *J. Chem. Phys.* **2013**, *138*, 184312.

- (35) Enami, S.; Colussi, A. J. Long-range specific ion-ion interactions in hydrogen-bonded liquid films. *J. Chem. Phys.* **2013**, *138*, 184706.
- (36) Enami, S.; Colussi, A. J. Ion-Specific Long-Range Correlations on Interfacial Water Driven by Hydrogen Bond Fluctuations. *J. Phys. Chem. B* **2014**, *118*, 1861–1866.
- (37) Jungwirth, P.; Tobias, D. J. Surface effects on aqueous ionic solvation: A molecular dynamics simulation study of NaCl at the air/water interface from infinite dilution to saturation. *J. Phys. Chem. B* **2000**, *104*, 7702–7706.
- (38) Omta, A. W.; Kropman, M. F.; Woutersen, S.; Bakker, H. J. Negligible effect of ions on the hydrogen-bond structure in liquid water. *Science* **2003**, *301*, 347–349.
- (39) Ghosal, S.; Hemminger, J. C.; Bluhm, H.; Mun, B. S.; Hebenstreit, E. L.; Ketteler, G.; Ogletree, D. F.; Requejo, F. G.; Salmeron, M. Electron spectroscopy of aqueous solution interfaces reveals surface enhancement of halides. *Science* **2005**, *307*, 563–566.
- (40) Knipping, E.; Lakin, M.; Foster, K.; Jungwirth, P.; Tobias, D.; Gerber, R.; Dabdub, D.; Finlayson-Pitts, B. Experiments and simulations of ion-enhanced interfacial chemistry on aqueous NaCl aerosols. *Science* **2000**, *288*, 301–306.
- (41) Otten, D. E.; Shaffer, P. R.; Geissler, P. L.; Saykally, R. J. Elucidating the mechanism of selective ion adsorption to the liquid water surface. *Proc. Natl. Acad. Sci. U.S.A.* **2012**, *109*, 701–705.
- (42) Petersen, P. B.; Saykally, R. J. On the nature of ions at the liquid water surface. *Annu. Rev. Phys. Chem.* **2006**, *57*, 333–364.
- (43) Onorato, R. M.; Otten, D. E.; Saykally, R. J. Measurement of bromide ion affinities for the air/water and dodecanol/water interfaces at molar concentrations by UV second harmonic generation spectroscopy. *J. Phys. Chem. C* **2010**, *114*, 13746–13751.
- (44) Smith, J. W.; Saykally, R. J. Soft x-ray absorption spectroscopy of liquids and solutions. *Chem. Rev.* **2017**, *117*, 13909–13934.
- (45) Baer, M. D.; Mundy, C. J. Toward an understanding of the specific ion effect using density functional theory. *J. Phys. Chem. Lett.* **2011**, *2*, 1088–1093.
- (46) Adel, T.; Ng, K. C.; Vazquez de Vasquez, M. G.; Velez-Alvarez, J.; Allen, H. C. Insight into the Ionizing Surface Potential Method and Aqueous Sodium Halide Surfaces. *Langmuir* **2021**, *37*, 7863–7874.
- (47) Beck, T. L. The influence of water interfacial potentials on ion hydration in bulk water and near interfaces. *Chem. Phys. Lett.* **2013**, *561*, 1–13.
- (48) Tobias, D. J.; Hemminger, J. C. Getting specific about specific ion effects. *Science* **2008**, *319*, 1197–1198.
- (49) Tielrooij, K.; Garcia-Araez, N.; Bonn, M.; Bakker, H. Cooperativity in ion hydration. *Science* **2010**, *328*, 1006–1009.
- (50) Consta, S.; Mainer, K. R.; Novak, W. Fragmentation mechanisms of aqueous clusters charged with ions. *J. Chem. Phys.* **2003**, *119*, 10125–10132.
- (51) Kwan, V.; O’Dwyer, R.; Laur, D.; Tan, J.; Consta, S. Relation between Ejection Mechanism and Ion Abundance in the Electric Double Layer of Droplets. *J. Phys. Chem. A* **2021**, *125*, 2954–2966.
- (52) Malek, S. M. A.; Poole, P. H.; Saika-Voivod, I. Thermodynamic and structural anomalies of water nanodroplets. *Nat. Commun.* **2018**, *9*, 2402.

- (53) Malek, S. M. A.; Poole, P. H.; Saika-Voivod, I. Surface tension of supercooled water nanodroplets from computer simulations. *J. Chem. Phys.* **2019**, *150*, 234507.
- (54) Johnston, J. C.; Molinero, V. Crystallization, melting, and structure of water nanoparticles at atmospherically relevant temperatures. *J. Am. Chem. Soc.* **2012**, *134*, 6650–6659.
- (55) Nandi, P. K.; Burnham, C. J.; Futera, Z.; English, N. J. Ice-amorphization of supercooled water nanodroplets in no man’s land. *ACS Earth Space Chem.* **2017**, *1*, 187–196.
- (56) Li, T.; Donadio, D.; Galli, G. Ice nucleation at the nanoscale probes no man’s land of water. *Nat. Commun.* **2013**, *4*, 1–6.
- (57) Haji-Akbari, A.; Debenedetti, P. G. Computational investigation of surface freezing in a molecular model of water. *Proc. Natl. Acad. Sci. U.S.A.* **2017**, *114*, 3316–3321.
- (58) Hall, K. W.; Zhang, Z.; Burnham, C. J.; Guo, G.-J.; Carpendale, S.; English, N. J.; Kusalik, P. G. Does local structure bias how a crystal nucleus evolves? *J. Phys. Chem. Lett.* **2018**, *9*, 6991–6998.
- (59) Rayleigh, L. XX. On the equilibrium of liquid conducting masses charged with electricity. *Philos. Mag.* **1882**, *14*, 184–186.
- (60) Peters, J. Rayleigh’s electrified water drops. *Eur. J. Phys.* **1980**, *1*, 143.
- (61) Hendricks, C.; Schneider, J. Stability of a conducting droplet under the influence of surface tension and electrostatic forces. *Am. J. Phys.* **1963**, *31*, 450–453.
- (62) Consta, S.; Malevanets, A. Disintegration mechanisms of charged nanodroplets: novel systems for applying methods of activated processes. *Mol. Simul.* **2015**, *41*, 73–85.
- (63) Consta, S. Manifestation of Rayleigh instability in droplets containing multiply charged macroions. *J. Phys. Chem. B* **2010**, *114*, 5263–5268.
- (64) Berendsen, H. J. C.; van der Spoel, D.; van Druren, R. GROMACS: A message-passing parallel molecular dynamics implementation. *Comput. Phys. Commun.* **1995**, *91*, 43.
- (65) Lindahl, E.; Hess, B.; van der Spoel, D. GROMACS 3.0: A package for molecular simulation and trajectory analysis. *J. Mol. Model.* **2001**, *7*, 306.
- (66) van der Spoel, D.; Lindahl, E.; Hess, B.; Groenhof, G.; Mark, A. E.; Berendsen, H. J. C. GROMACS: Fast, Flexible and Free. *J. Comput. Chem.* **2005**, *26*, 1701.
- (67) Hess, B.; Kutzner, C.; van der Spoel, D.; Lindahl, E. GROMACS 4: Algorithms for highly efficient, load balanced, and scalable molecular simulation. *J. Chem. Theory Comput.* **2008**, *4*, 435.
- (68) Phillips, J. C.; Braun, R.; Wang, W.; Gumbart, J.; Tajkhorshid, E.; Villa, E.; Chipot, C.; Skeel, R. D.; Kalé, L.; Schulten, K. Scalable molecular dynamics with NAMD. *J. Comput. Chem.* **2005**, *26*, 1781–1802.
- (69) Abascal, J. L. F.; Vega, C. A general purpose model for the condensed phases of water: TIP4P/2005. *J. Chem. Phys.* **2005**, *123*, 234505.
- (70) González, M. A.; Valeriani, C.; Caupin, F.; Abascal, J. L. F. A comprehensive scenario of the thermodynamic anomalies of water using the TIP4P/2005 model. *J. Chem. Phys.* **2016**, *145*, 054505.
- (71) Vega, C.; de Miguel, E. Surface tension of the most popular models of water by using the test-area simulation method. *J. Chem. Phys.* **2007**, *126*, 154707.
- (72) Vega, C.; Abascal, J. L. F.; Nezbeda, I. Vapor-liquid equilibria from the triple

- point up to the critical point for the new generation of TIP4P-like models: TIP4P/Ew, TIP4P/2005, and TIP4P/ice. *J. Chem. Phys.* **2006**, *125*, 034503.
- (73) Lamoureux, G.; Harder, E.; Vorobyov, I. V.; Roux, B.; MacKerell, A. D. A polarizable model of water for molecular dynamics simulations of biomolecules. *Chem. Phys. Lett.* **2006**, *418*, 245–249.
- (74) Yu, H.; Whitfield, T. W.; Harder, E.; Lamoureux, G.; Vorobyov, I.; Anisimov, V. M.; MacKerell, A. D.; Roux, B. Simulating Monovalent and Divalent Ions in Aqueous Solution Using a Drude Polarizable Force Field. *J. Chem. Theory Comput.* **2010**, *6*, 774–786, PMID: 20300554.
- (75) Luo, Y.; Jiang, W.; Yu, H.; MacKerell, A. D.; Roux, B. Simulation study of ion pairing in concentrated aqueous salt solutions with a polarizable force field. *Faraday Discuss.* **2013**, *160*, 135–149.
- (76) Humphrey, W.; Dalke, A.; Schulten, K. VMD: Visual Molecular Dynamics. *J. Mol. Graphics* **1996**, *14*, 33–38.
- (77) Chau, P. L.; Hardwick, A. J. A new order parameter for tetrahedral configurations. *Mol. Phys.* **1998**, *93*, 511–518.
- (78) Aragoles, J. L.; MacDowell, L. G.; Vega, C. Dielectric Constant of Ices and Water: A Lesson about Water Interactions. *J. Phys. Chem. A* **2010**, *115*, 5745–5758.
- (79) Chandler, D. *Introduction to modern statistical mechanics*; New York, Oxford University Press, 1987.
- (80) Gladich, I.; Roeselová, M. Comparison of selected polarizable and nonpolarizable water models in molecular dynamics simulations of ice I_h. *Phys. Chem. Chem. Phys.* **2012**, *14*, 11371–11385.
- (81) Muchova, E.; Gladich, I.; Picaud, S.; Hoang, P. N.; Roeselova, M. The Ice-Vapor Interface and the Melting Point of Ice I_h for the Polarizable POL3 Water Model. *J. Phys. Chem. A* **2011**, *115*, 5973–5982.
- (82) Vrbka, L.; Jungwirth, P. Homogeneous freezing of water starts in the subsurface. *J. Phys. Chem. B* **2006**, *110*, 18126–18129.
- (83) Peters, K. F.; Chung, Y.-W.; Cohen, J. B. Surface melting on small particles. *Appl. Phys. Lett.* **1997**, *71*, 2391–2393.
- (84) Tsironi, I.; Schlesinger, D.; Späh, A.; Eriksson, L.; Segad, M.; Perakis, F. Brine rejection and hydrate formation upon freezing of NaCl aqueous solutions. *Phys. Chem. Chem. Phys.* **2020**, *22*, 7625–7632.
- (85) Vrbka, L.; Jungwirth, P. Brine rejection from freezing salt solutions: A molecular dynamics study. *Phys. Rev. Lett.* **2005**, *95*, 148501.
- (86) Elliott, S. R. Medium-range structural order in covalent amorphous solids. *Nature* **1991**, *354*, 445–452.
- (87) Shi, R.; Tanaka, H. Distinct signature of local tetrahedral ordering in the scattering function of covalent liquids and glasses. *Sci. Adv.* **2019**, *5*, eaav3194.
- (88) Saika-Voivod, I.; Smalenburg, F.; Sciortino, F. Understanding tetrahedral liquids through patchy colloids. *J. Chem. Phys.* **2013**, *139*, 234901.
- (89) Wei, X.; Miranda, P. B.; Shen, Y. Surface vibrational spectroscopic study of surface melting of ice. *Phys. Rev. Lett.* **2001**, *86*, 1554.
- (90) Sánchez, M. A.; Kling, T.; Ishiyama, T.; van Zadel, M.-J.; Bisson, P. J.; Mezger, M.; Jochum, M. N.; Cyran, J. D.; Smit, W. J.; Bakker, H. J. et al. Experimental and theoretical evidence for bilayer-by-bilayer surface melting of crystalline ice. *Proc. Natl. Acad. Sci. U.S.A.* **2017**, *114*, 227–232.